Two types of slab components under Ecuadorian volcanoes supported by primitive olivine-hosted melt inclusion study

Diego Narvaez, Pablo Samaniego, Kenneth T. Koga, Estelle F. Rose-Koga, S. Hidalgo, Gueorgui Ratzov

Two types of slab components under Ecuadorian volcanoes supported by primitive olivine-hosted melt inclusion study

D.F. Narváez[a,b], P. Samaniego[a], K.T. Koga[a], E.F. Rose-Koga[a], S. Hidalgo[c], G. Ratzov[d]

[a] Université Clermont Auvergne, CNRS, IRD, OPGC, Laboratoire Magmas et Volcans, F-63000 Clermont-Ferrand, France
[b] Departamento de Geología, Facultad de Ingeniería en Geología y Petróleos, Escuela Politécnica Nacional, Quito, Ecuador
[c] Instituto Geofísico, Escuela Politécnica Nacional, Ladrón de Guevara E11-253, Aptdo. 2759, Quito, Ecuador
[d] Université Côte d'Azur, CNRS, IRD, Observatoire de la Côte d'Azur, Géoazur, 250 rue Albert Einstein, Sophia Antipolis 06560 Valbonne, France

Corresponding author: Diego F. Narváez (diego.narvaez@epn.edu.ec; ORCID ID: 0000-0003-1902-2472)

Abstract

The origin of several geochemical parameters in continental arc lavas (e.g., La/Yb, Ba/Th) is controversial as to whether it is imparted by the slab or acquired in the crust. In Ecuador, where volcanoes are built over a thick crust (~50 km), this problem is grounded in the lack of primitive rocks. Here, we use melt inclusions hosted in Fo_{80-90} olivines to decipher the slab component signatures that metasomatises the sub-arc mantle. We report major, trace, and volatile elements analyzed in experimentally heated melt inclusions, which are from primitive rocks of Cotacachi, Cubilche, Cono de la Virgen, Conos de Licto, and Sangay volcanoes located in the north and south of the Ecuadorian arc. Based on trace element data and geochemical modelling, we recognize two types of slab components: one is indicative of aqueous fluids (e.g., high Ba/La, Pb/Ce, B/Nb), and the other is indicative of hydrous siliceous melts (e.g., high La/Nb, Th/Nb). The aqueous fluid signature is recognized in all volcanoes (except for Cono de la Virgen), and their F/Cl are distributed around 0.43±0.07, independent of the distance to the Benioff zone. We propose a model where hydrous siliceous melts result from the subduction of a young oceanic crust north of the Grijalva fracture zone. Additionally, we show that the mantle under Licto and Sangay volcanoes is enriched prior to metasomatism by slab fluids. This study shows that melt inclusions give valuable insights into the composition of primitive melts that are rarely accessible as whole rocks.

Key words: primitive magma, subduction zone, trace element, mantle metasomatism, Northern Volcanic Zone, Andes

1 Introduction

The partial melting to form arc magmas is thought to be triggered by fluids and melts derived from the subduction slab. Here, the fluids and melts are termed the slab component. The slab component imparts the incompatible trace element arc signature (Davidson, 1996; Pearce and Peate, 1995; and references therein), and together with the mantle and the crust, contributes to the final geochemical character of arc magmas (e.g. Elliot et al., 1997; Streck et al., 2007). Defining the geochemical slab component signature is a challenging task because magmas change their compositions during their ascent through the crust, which hinder or overprint the slab and mantle contributions. Whereas some arc magma trace element characteristics, such as a depletion in high-field-strength elements (HFSE, i.e. Nb, Ta) and an enrichment in large-ion-lithophile elements (LILE, i.e. Th, Rb), is often ascribed to the slab component signature (Elliot et al., 1997; Pearce and Peate, 1995), other geochemical parameters (i.e., high Sr/Y, La/Yb, Th/La) can be acquired in the crust or imparted by the slab. This geochemical complexity has led to a long-lasting discussion about the role of the slab and the crust components in the chemistry of arc magmas (e.g., Elliott et al., 1997; Plank, 2005; Rogers and Hawkesworth, 1989).

When the slab component can be identified, it also gives insight into the dehydration and melting processes occurring in the subducting slab (e.g., Davidson, 1996). The current "paradigm" states that aqueous fluids are most probably related to slab dehydration, occurring principally along low-temperature subduction zones (e.g. Leeman and Sisson, 1996), while hydrous siliceous melts are likely related to the partial melting of the subducting slab (which includes both the altered oceanic crust and the overlying sediments) along high-temperature subduction zones (Elliott et al., 1997, Hermann and Rubatto, 2009).

Recent experimental studies have focused on the determination of the efficiency of the slab component in moving incompatible elements from the slab to the mantle wedge. These studies demonstrate that the slab component changes its property depending on the temperature at which the transport takes place (i.e. Carter et al., 2015; Hermann and Rubatto, 2009; Kessel et al., 2005). For example, Hermann and Rubatto (2009) and Carter et al. (2015), who analyzed the hydrous melts produced at high temperature during wet melting of sediments and basalts, respectively, have shown that the concentration of key trace elements in the melt (i.e. Zr, Y, rare earth elements (REE)) increases with temperature. However, the degree of enrichment is not the same for all the elements, because their concentration is controlled by the residual phases that host such key elements. Thus, if the hosting phase is exhausted during melting, the elements contained in that phase reach a maximum concentration at the temperature of exhaustion. As a result, the behavior of some elements during slab melting is controlled by minor and accessory phases, as for example: light REE (LREE) and Th is controlled by epidote and monazite, Zr by zircon, Rb by phengite, and Nb and Ta by rutile. Similar to that occurred with melts, the concentration of some key trace elements also increases with temperature in aqueous fluids produced by sediments below the solidus (Spandler et al., 2007), although their maximum concentration is lower than that measured in melts. An additional complexity has been highlighted by Rustioni et al. (2019), who have shown that the capacity of fluids for transporting trace elements is not only a temperature-dependent property, but it can also be enhanced by the presence of large amounts of chlorine (> 5 wt.%) in the slab-derived fluids. The geochemical

characters of slab components are therefore derived from the composition of lithology (i.e. sediments, AOC) and the element fractionation between major or accessory minerals and fluid or melt. Despite such complexity, the trace element abundance in the slab-derived fluids or melts increase with temperature, and therefore melts are better carriers of trace elements that their low-temperature counterparts. This study focuses on this first-order characteristic to interpret geochemical signature of arc magmas, then evaluate contributions of others with quantitative modelling.

In the Ecuadorian segment of the Northern Volcanic Zone of the Andes– "Ecuadorian Arc" – the slab contribution recorded in basaltic andesites and andesites with low Ba/Th, high La/Yb, and high Th/La has been debated for several years. Some studies propose that such geochemical signatures are imprinted into the sub-arc mantle by hydrous siliceous melts coming from the slab melting, and these signatures persist until the magmas reach the surface due to low degrees of crustal contamination (e.g., Ancellin et al., 2017; Hidalgo et al., 2012; Samaniego et al., 2005). On the other hand, other authors propose that the slab component is an aqueous fluid, and therefore the high La/Yb and Th/La are acquired in the crust due to hornblende and (or) garnet crystallization and crustal assimilation (e.g., Chiaradia et al., 2020). In this work, we will discuss the origin of the slab component, based on the dichotomy fluids and melts. In contrast, we discard the involvement of saline fluids in the Ecuadorian subduction system because salt deposits have not been reported in the subducted sediment layer (see below).

In this work, we studied melt inclusions (MI) hosted in Fo_{80-90} olivines from whole rocks in which Mg# [defined as molar 100*Mg/(Mg+Fe_T)] was greater than 55. We selected those rocks in order to focus our effort on the most primitive melts – those less affected by crustal processes – from the Ecuadorian arc. The sampled rocks came from Cono de la Virgen (CLV), Cotacachi, and Cubilche volcanoes that are located in the northern part of the Ecuadorian arc, and from Conos de Licto (Licto) and Sangay volcanoes, located in the southern part of the Ecuadorian arc (Fig. 1). We also compiled MI data from the literature from Pan de Azúcar (PDA), Rucu Pichincha (Le Voyer et al. 2008), and Puñalica volcanoes (Narváez et al., 2018, see Fig. 1). We used ratios of incompatible trace elements in MI to avoid the effect of fractional crystallization, and we demonstrated: (1) that their chemical variability was not acquired in the crust, and (2) that MI compositions resulted from melting of mantle that has been metasomatised by both aqueous fluids and (or) hydrous siliceous melts. Also, we gave some insights about the composition of the sub-arc mantle beneath Ecuador and interpreted the geochemical MI signature, for example, F/Cl ratio, in the context of the geodynamical setting of the Ecuadorian arc.

2 General information on the Ecuadorian arc and sample descriptions

2.1 The Ecuadorian arc: geodynamic setting and geochemical summary

The Andean Northern Volcanic Zone (NVZ) spans from Northern Colombia (~6°N) to Central Ecuador (~2°S) and results from the oblique convergence of the Nazca and the South American plates, at a rate of 5-6 cm/year (Nocquet et al., 2014). In Colombia (6°N to 2°N), the Nazca plate subducts at a 30°-40° dip to the east, while in Southern Ecuador and Northern Peru (between ~3°S and 8°S), the Nazca plate subducts at a ~10º dip, defining the Peruvian flat slab (Yepes et al., 2016, and references therein). In Northern and Central Ecuador, the subducting slab contains two significant structures. The first is the Carnegie ridge (located between 0° and 3°S), which is a 200-250 km-wide, 2 km-high submarine mountain range (Fig. 1a) originating from Galápagos hotspot activity. The Carnegie ridge is responsible for the low angle of subduction (~25° dip) of the Nazca plate at this latitude due to its higher buoyancy (Yepes et al., 2016). The second structure is the N60ºE Grijalva fracture zone (GFZ, Fig. 1a), which consists of a 500 m-high escarpment separating an older subducting slab (25-30 Ma) to the south, from a younger oceanic crust (12-20 Ma) to the north (Yepes et al., 2016). One important feature of Ecuadorian volcanoes is their location with respect to GFZ. Among the volcanoes studied, Licto and Sangay are the only volcanoes located south of GFZ while the others are located just above or to the north of GFZ.

The width (east-west) of the Ecuadorian arc is greater (~120 km) than that of the volcanic arc in Colombia (40-50 km) and is characterized by more than 80 Quaternary volcanic centers (Hall et al., 2008) constructed on a heterogeneous, 50-55 km thick continental crust (Koch et al., 2021). Those volcanoes are distributed along four alignments based on their location with respect to the two principal mountain ranges (the Western and Eastern Cordilleras, see topographic profile in Fig. 1d). The frontal and the main arc groups correspond to volcanoes located above the Western and Eastern Cordilleras, respectively. Volcanoes from the frontal arc lie upon Meso-Cenozoic volcanic and sedimentary rocks of oceanic affinity (Vallejo et al., 2009), while those from the main arc are constructed over a continental-like crust that consists of felsic and intermediate igneous and metamorphic rocks (Litherland et al., 1994). The third group corresponds to the volcanoes of the Inter-Andean valley, which are constructed above Miocene and Pliocene volcanic and sedimentary rocks (Winkler et al., 2005). Finally, a few scarce volcanoes that are further east constitute the Sub-Andean zone group and are in the upper Amazon basin.

The geochemical studies performed over the last two decades on Quaternary Ecuadorian volcanic rocks describe the main geochemical characteristic of this arc segment. First of all, the magma composition changes from the west to the east (across-arc) by an increase in incompatible trace elements and a decrease in LILE over HFSE ratios further from the trench. This feature is usually interpreted as resulting from a decrease in the amount of fluids added into the sub-arc mantle from the subducting slab, and consequently, a decrease of mantle melting (Barragán et al., 1998; Hidalgo et al., 2012). More recently, significant north-south (along-arc) geochemical variations have been described and are associated with a change in the slab

component composition (Ancellin et al., 2017), or with a distinctive depth of magma-crust interactions (Chiaradia et al., 2020). In addition, Ecuadorian magmas broadly display an adakitic signature, mostly defined by high La/Yb and Sr/Y values. These compositions, mostly recognized in frontal arc volcanoes located between 0.5ºN and 1ºS, have been interpreted either in terms of partial melting of the slab and the subsequent metasomatic reactions in the mantle wedge (Hidalgo et al., 2012; Samaniego et al., 2005), or as due to lower crustal processes associated with high-pressure fractionation and (or) melting (Chiaradia et al., 2020).

2.2 Sample locations

Cotacachi volcano (78.34ºW, 0.36ºN, 4944 m above sea level – asl, Fig. 1b), located in the Western Cordillera, is a Late Pleistocene stratovolcano formed by two successive edifices (Cotacachi I and II; Almeida, 2016). The oldest edifice comprises the outermost part of the present cone and is formed by basaltic andesite and andesitic lavas. Cotacachi II includes a sequence of andesitic lavas present on the upper part of Cotacachi and four dacitic satellite domes constructed on the lower Cotacachi I flanks. The three studied samples (17EQ91, MM1B, COTA02) come from Cotacachi I edifice and are calc-alkaline basaltic andesite lavas and one pyroclastic bomb (Table 1).

Cubilche volcano (78.13ºW, 0.23ºN, 3826 m asl) is a Late Pleistocene edifice (40-45 ka, Bablon et al., 2020), located in the Inter-Andean valley, that displays a horseshoe-shaped amphitheater opened to the north resulting from a sector collapse. It comprises two volcanic edifices named Old and Young Cubilche (Navarrete et al., 2020). The two studied samples come from Old Cubilche (17EQ81, 17EQ95) which are black, vesiculated, calc-alkaline andesitic lavas.

Cono de la Virgen – CLV – (77.91ºW, 0.02ºN, 3673 m asl) is a recent, Holocene satellite edifice associated with the Cayambe volcanic complex (Samaniego et al., 2005) and located on the Eastern Cordillera. This cone has a 250-300 m-thick succession of high-K calc-alkaline andesite lava flows. We selected three samples from the distal lava flows (CAY45A, CAY45B, CAY45C).

Conos de Licto – Licto – (78.62ºW, 1.78ºS) are two scoria cones with adjacent lava flows located in the southern part of the inter-Andean valley. The cones are aligned (N74°W) and are named Cerro Tulabug and Loma Bellavista. RIO10B was a lava flow sample of basaltic-andesite composition. This sample comes from a lava related to Cerro Tulabug (3336 m asl) that is dated at 183 ± 9 ka (Bablon et al., 2019).

Sangay volcano (78.34ºW, 2.00º S, 5230 m asl) is the southernmost active edifice of the NVZ and is located on the Eastern Cordillera. It was constructed over the last 500 ka by three successive edifices (Sangay I, II and III; Monzier et al., 1999), which are separated by two major sector collapses. Sangay I growth extended from 500 to 250 ka, Sangay II from 100 to 50 ka, and the present cone has been active for at least 14 ka. The rock compositions span from basaltic andesites to dacites. One basalt is reported in the Sangay II sequence, and its olivine-hosted MI

were previously studied by Narváez et al. (2018). The selected sample for current work, SAN21B, is from Sangay II edifice, and it is a calc-alkaline basaltic andesite lava.

Compiled MI data are from Rucu Pichincha, PDA, and Puñalica volcanoes. *Rucu Pichincha* volcano (0.85-0.2 Ma) is one of the two edifices that compose the Pichincha volcanic complex (Robin et al. 2010) and is located on the Western Cordillera. *PDA* is a poorly known stratovolcano from the Sub-Andean zone that is hardly accessible due to its location in the Amazon jungle. One basaltic andesite from Rucu Pichincha and one basaltic lava from PDA were studied by Le Voyer et al. (2008). *Puñalica* is a 300 m-high cone-shape edifice located on the Western Cordillera. A distal lava flow from this edifice was dated at 18 ± 3 ka (Bablon et al., 2019). Four bombs and lavas from Puñalica volcano were studied by Narváez et al. (2018) and range from basaltic andesite to andesite in composition.

2.3 Offshore sediment samples

We also analyzed oceanic sediments that were sampled in sedimentary piston cores collected in the Manglares Forearc Basin (Collot et al., 2019) on the North Ecuador margin slope and subduction trench (Ratzov et al., 2010) (Fig. 1c). These sediments are related to the Esmeraldas submarine canyon, which is located immediately north of the Carnegie ridge collision zone. This submarine canyon incises the continental shelf and serves as a conduit for particle transport from the continent to the trench. The sediment contribution is probably recurrent since the beginning of the incision of this canyon (~5.3 Ma ago, Collot et al., 2019). These sediments were collected during the AMADEUS oceanographic cruise at water depths ranging between 606 m below sea level (bsl) and 3797 m bsl (Table 2). These data were crucial for magma genesis discussion and geochemical modeling. The samples included both (1) hemipelagic deposits mainly composed of greenish brown-silty clay, with few fragments of wood and foraminifera, and (2) coarser silty turbidites that reflect the erosion of the arc and forearc by major rivers, or submarine slope failures of the margin sedimentary cover during earthquakes (Ratzov et al, 2010). Additionally, for the discussion of magma genesis we used the bulk sediment composition reported by Plank (2014), which corresponds to siliceous nannofossil ooze of pelagic origin. This sediment was sampled ~400 km off the coast of Ecuador during the deep-sea drilling project (leg 62 site 504, Cann et al., 1983) and represent an additional sediment type that is subducted in front of Ecuador.

3 Methods

3.1 Olivine-hosted melt inclusion preparation

We crushed 9 lavas and one volcanic bomb and separated the 0.4-1.5 mm fraction. We picked olivine crystals under a binocular microscope. Then, we selected olivines with MI bigger than 25 µm in diameter. MI were typically sub-spherical to elongate, rounded, and between 25-300 µm in diameter (detailed dimensions were noted in extended Table 3 available on EarthChem library, https://doi.org/10.26022/IEDA/111625). All MI were partially crystalized and presented bubbles; therefore, we performed a heating procedure using a Vernadsky-type

microscope heating stage at 1-atm (Sobolev et al., 1980) following the method described by Le Voyer et al. (2008). The heating procedure followed these steps: an increase in the temperature of an olivine crystal (containing one or more MI) from a room temperature up to the temperature for melting crystals inside the MI, in order to reverse the crystallization that occurred after MI entrapment. For each experiment, the temperature was increased at a rate of 80°C/min until the heating stage reached the Au melting point (1064 °C), then at 10-30°C/min. The oxygen fugacity was kept below 10^{-10} bars at 1200°C (nickel-nickel oxide buffer of -7.5) to avoid oxidation of the host mineral. Once we observed the disappearance of all minerals inside the MI, we kept the temperature constant for 5 min and quenched the experiment by turning off the electric current to the heater. The whole procedure was completed in less than 30 minutes. The MI were visually monitored during the entire heating procedure with a microscope (*cf.* Sobolev et al., 1980). Generally, one or more bubbles were present inside the MI at the beginning of the experiments. Bubbles moved and often coalesced during heating, and they remained after quenching. After the experiment, the bubble sizes ranged from 10 to 100 µm, and on average represented 8 vol.% of MI. We polished 67 olivines with silicon carbide papers to expose the quenched MI, and we used alumina powder for the final polish.

3.2 Analytical methods

Major and trace element compositions of olivine crystals and MI were analyzed at Laboratoire Magmas et Volcans (LMV, Clermont-Ferrand, France) using a CAMECA SX100 electron microprobe and a Laser Ablation Inductively Coupled Plasma Mass Spectrometer (LA-ICP-MS), respectively. We performed the volatile element analysis by secondary ion mass spectrometry (SIMS) before the LA-ICP-MS but after the electron microprobe analysis.

For major elements, the standard analytical procedure was reported in detail in Le Voyer et al. (2008). Olivine analyses were performed with a focused beam, at 15 kV accelerating voltage, a current of 15 nA, and 10 seconds counting time for each element. Glasses were analyzed with a beam of 5-20 µm in diameter (depending on the diameter of the MI), a low current (8 nA) for major elements, and 80 nA for Cl, S, and F (Rose-Koga et al., 2014). No alkali loss was detected on the natural basaltic glass VG-A99 (supplementary material table S1) under these beam conditions, and alkalis of all MI (except for three MI from CLV) plotted along expected liquid lines of descent, which suggest no alkali loss.

For trace elements, we used a laser ablation system (193 nm Eximer Resonetics M-50E) coupled with an inductively coupled plasma mass spectrometer (Agilent 7500 cs) following the procedure outlined in previous studies (Rose-Koga et al., 2014). To summarize, we used a pulse energy of ~3 mJ, a spot diameter between 15 and 33 µm, and a laser pulse frequency of 2-3 Hz depending on the inclusion size, ensuring a fluence at sample surface of ~4 J/cm^{-2}. The background was measured for 40 seconds before ablation, and the analysis time was approximately 100 seconds. Data reduction was performed using GLITTER software. We used BCR-2G and NIST SRM 612 basaltic glasses (for details see supplementary material supplementary table S2) as standard samples and Ca as the reference element. Typical errors on

the MI (1σ error of mean, $1/\sqrt{n}$ where n is the number of cycles) were less than 15% for all trace elements, except for Ta (<25%), and B (<40%).

We measured volatiles (F, S, Cl) in the MI using the CAMECA HR1280 housed at Centre de Recherches Pétrographiques et Géochimiques (CRPG, Nancy, France). We used SIMS settings similar to those detailed in other studies (e.g., Rose-Koga et al., 2014) and summarized below. We used a Cs^+ primary ion beam with a current of 1 nA, a 10 kV secondary accelerating voltage, a -80 V offset, and a projected beam size of 10-20 µm. The instrument was operated with the contrast aperture at 400 µm, the energy aperture at 40 eV, the entrance slit at 52 µm, and the exit slit at 173 µm for a mass resolution power of 7007, enough to separate all mass interfering signals. The standard basaltic glasses used during SIMS analysis were KL2G, VG2, and 47963-b (for details see supplementary material table S3), and the relative standard deviations on MI were, in general, <20% for Cl; and <10% for F and S.

Lava samples from Cotacachi and Cubilche volcanoes, as well as five samples of sediments from the Ecuadorian subduction trench and Manglares forearc basin were analyzed following the analytical procedure detailed in Cotten et al. (1995). Rock samples were crushed in agate grinder. Major and trace elements were measured by inductively coupled plasma-atomic emission spectrometry (ICP-AES) using a Horiba Jobin Yvon® Ultima 2 spectrometer, at the Université de Bretagne Occidentale (Brest, France). For major elements, the relative standard deviations were ≤1% for SiO_2, ≤2% for other major elements, and ≤5% for trace elements.

4 Results

The following description of major, trace, and volatile elements only concern new data. MI data from Rucu Pichincha, PDA, Puñalica and Sangay (SAN20B shown in pink triangles in figures) are extensively compared with the new data, but they are not reported in this section. The details are found in Le Voyer et al. (2008) and Narváez et al. (2018).

4.1 Major and trace elements

The MI are mostly low in silica (41.6-53.9 wt.% SiO_2, Fig. 2), and range from sub-alkalic to alkalic, with K_2O ranging widely, from medium-K calc-alkaline to shoshonitic compositions. In general, for all MI compositions, MgO, FeO_T, CaO and TiO_2 produce a negative correlation with SiO_2, while Na_2O, K_2O and Al_2O_3 display a positive trend (Fig. 2b, d).

All the studied MI display a typical arc signature based on their trace element abundance pattern (Fig. 3) and are characterized by an enrichment in LILE (e.g., Ba, Sr) relative to HFSE (e.g., Nb, Ta). It is noteworthy that all MI have similar compositional ranges to their host-lavas, except for MI from CLV that show higher concentrations than its host lava.

The fractionation between LREE and heavy REE (HREE) is weak in Cotacachi and Cubilche MI, and the element abundances normalized to a primitive mantle display relatively

flat or low-slope REE patterns (Fig. 3a, b). Such a feature is represented by low values of $(La/Yb)_N$ (normalized to the primitive mantle values of McDonough and Sun (1995), Table 4). On the other hand, CLV MI show very steep REE patterns with high $(La/Yb)_N$ values (up to 140) and correspond to the highest values so far reported in olivine-hosted MI in the Ecuadorian arc (*cf.* Le Voyer et al., 2008; Narváez et al., 2018). The REE patterns of all the other MI (Licto, Puñalica, Sangay, PDA) display intermediate concentrations. CLV MI also show the highest concentration in trace elements (Fig. 3e) compared to other MI from this arc segment (except for Ta, Ti, Y, Yb and Lu).

Trace element compositions from Cotacachi and Cubilche MI showed several similarities. For instance, MI from both volcanoes are enriched in fluid-mobile elements compared to HFSE (e.g., B/Nb, Table 4) and LILE relative to LREE (e.g., Ba/La and Pb/Ce), and they are richer in Ti, Eu, and poorer in Th compared to whole-rock compositions of their host lavas (Fig. 3b, c).

Sangay and Licto MI display intermediate $(La/Yb)_N$ values, and their trace element composition is very similar to one another (Fig. 3g). This set of MI has lower Ba/La and Pb/Ce values than MI from Cubilche and Cotacachi but higher than those from CLV (see Table 4). A remarkable feature of Sangay and Licto MI are their Nb-enrichment, represented by a less prominent negative Nb-anomaly (Fig. 3c, d), yielding a higher Nb/Nb* value between 0.1 and 0.17 [log(Nb*) = ((log(U)+log(K))/2), normalized to NMORB], compared to Cubilche, Cotacachi, and CLV MI with Nb/Nb* ranging from 0.03 to 0.1.

4.2. Volatile elements

MI from all volcanoes, except for CLV, have similar Cl (503-1991 ppm), F contents (283-491 ppm) and S (0.052 to 0.26 wt.%). MI from CLV have lower Cl (305-1018 ppm) and display the highest F contents (1703-2969 ppm) reported so far in Ecuadorian MI (Fig. 4). As in the case for F, MI from CLV show the highest concentrations of S (0.3 to 0.65 wt.%). In general, S in MI are partitioned in the fluid phase (bubble, e.g., Bucholz et al., 2013), therefore the reported MI concentrations of S are different from those present in the melt at the time of entrapment and must be considered as minimum values. On the contrary, F and Cl concentrations in MI are better preserved at the time of entrapment, because they are less affected by diffusion (Bucholz et al., 2013), because they have low degassing pressure (100 and 10 MPa, respectively, Spilliaert et al., 2006), and because a small amount of fluid exsolution from melt (degassing) does not change F and Cl concentration in melt (e.g. SolEx model, Witham et al., 2012; natural degassing trend Spilliart et al., 2006).

5 Discussion

5.1 Limitations of post-entrapment modification corrections

Major and volatile element concentrations measured in MI rarely represent the composition of the melt at the time of entrapment because they change during cooling of host lavas and during experimental heating. The heating stage homogenization is considered to bring

the MI closer to the composition of entrapment (Le Voyer et al., 2008) by reversing crystallization. However, there are other processes that modify MI composition after its entrapment. For example, Fe and Mg can be modified due to re-equilibration with the host olivine via diffusion of Fe out of and Mg into the MI (Danyushevsky et al., 2000). Also, Si depletion in MI can be caused by incorporation of silica and H^+ in the olivine structure through crystallization of metal-defect olivine (Portnyagin et al., 2019). Such MI-olivine interactions are potentially significant during magma cooling in the crust over a time period that is several orders of magnitude longer than the laboratory heating procedure. After careful examination of proposed corrections of these Fe, Mg, and Si modifications, it was not possible to reconstruct the major element composition of our MI accounting for post-entrapment modifications (PEM) without making assumptions on the initial FeO_T and SiO_2 concentrations, values that in our case are not known. We concluded that the data presentation would be less biased using the measured MI data as is, without any correction for PEM. We chose to present uncorrected data in this paper and consider such data presentations to negligibly affect the following discussions of geochemical systematics of trace elements ratios, as incompatible trace elements have lower diffusion coefficients (i.e., REE) compared to Mg, Fe, and water (Cherniak, 2010).

5.2 Composition of Ecuadorian primitive magmas

5.2.1 The primitive magmas beneath Ecuador and the magmatic processes affecting them

Quaternary rocks from the Ecuadorian arc typically display silica contents higher than 52 wt.% (*cf.* database from Ancellin et al., 2017 and Hidalgo et al., 2012). Among this large database (~1500 rock analyses), few magnesian rocks (Mg#>55) bearing high-forsterite olivines ($Fo_{>80}$) have been reported. The most common minerals are plagioclase, orthopyroxene, clinopyroxene, and amphibole, with biotite and some rare quartz present in evolved rocks (Hall et al., 2008). Rocks from the sub-Andean zone are mainly basanites and tephrites showing Na-pyroxene and hauyne (Barragan et al., 1998; Hoffer et al., 2008). Here, we stress that, for this study, we selected rare high-forsterite olivines (Fo_{80-90}) hosted in rocks with Mg#>55 from the frontal arc, the inter-Andean valley, and the main arc. They are therefore a small subset representing the most mafic olivine-bearing lavas found in Ecuador, and thus the MI sampled in such mafic lavas allowed us to study the most primitive magmas of the Ecuadorian arc that are not otherwise accessible.

We calculated the olivine compositions in equilibrium with their host-rocks using olivine-melt equilibrium model of Ford et al. (1983) and compared them to natural olivine compositions. Thus, we confirmed that olivine phenocrysts from Cotacachi (Fo_{84-88}) and Sangay (Fo_{81-84}) are in equilibrium with their host-rock (forsterite content of equilibrium-olivine is 85.9 and 82.8, respectively). On the contrary, olivine phenocrysts from Cubilche, CLV and Licto are not. Olivines from Cubilche and CLV have higher forsterite content (84-88 and 86-90, respectively) than the expected equilibrium-olivines (83.4 for Cubilche and 86.0 for CLV) which means that such olivines crystalized from a more primitive magma. On the other hand, olivine

phenocrysts from Licto show lower forsterite content (83-86) than expected olivine (87-89), meaning that their host lava composition is the result of olivine accumulation. However, Cubilche, CLV and Licto MI show similar trace element patterns and similar trace element concentrations to their host lavas (Fig. 3). Because of this, olivines from Cubilche, CLV and Licto must be considered antecrysts, which are crystals coming from a magma genetically related to the one they are found.

Magmatic processes such as fractional crystallization, assimilation, and magma mixing could affect trace element composition of magmas after their formation in the mantle prior to entrapment in olivine crystals. To identify the main process affecting trace elements, we used an approach similar to that of Allègre and Minster (1978), which aims to rule out the effect of fractional crystallization and discuss the significance of partial melting and magma mixing in primitive magmas. For this, we plotted MI in a diagram of C_H/C_M versus C_H, where C_H and C_M are the concentrations of a highly incompatible (e.g., Rb, Th, U, Ta) and moderately incompatible (e.g., Nd, Zr) element, respectively. Compositions that plot along a straight line with a slope greater than zero are consistent with a partial melting process, while those that plot along a horizontal line are consistent with fractional crystallization. In this diagram, magma mixing process lie along a hyperbolic curve, rendering discrimination between partial melting and magma mixing a challenging task. In any case, we would stress that both processes (partial melting and magma mixing) are more effective in changing C_H/C_M than fractional crystallization.

In Fig. 5 we plotted the MI for the studied volcanoes together with the corresponding whole-rock (WR) fields. All MI (except for CLV) plot along two different straight lines of positive slope, corresponding to Cotacachi-Cubilche and Sangay-Licto trends. Puñalica MI have higher Th and Rb values than Sangay-Licto trend and probably form an independent group towards CLV MI. It is worth noting that WR for these volcanoes extend the MI fields toward greater Th and Rb, with the Sangay-Licto samples extending Th and Rb in a greater way than those of the Cotacachi-Cubilche for a given (Th, Rb)/Nd values. We stress that the differences observed in WR are also present for MI, indicating that such geochemical systematics is a characteristic of primitive melts (represented by MI). Given that these trends display a positive slope, we conclude that fractional crystallization is not the main process controlling their trace element geochemistry. Therefore, these systematics must be explained by other processes such as partial melting or magma mixing. The partial melting of a mantle source of similar composition produces melts that plot along a single line, which is the case of Cotacachi and Cubilche or Sangay and Licto MI. The difference in Th and Rb of Cotacachi-Cubilche compared to Sangay-Licto trends (Fig. 5a, b) therefore must indicate a difference in the composition of the metasomatized mantle source. We should also stress that other additional geochemical parameters are similar in MI as in WR (i.e., Zr/Nb, Rb/Nb, La/Nb, supplementary material text S1 and Fig. S2) which indicates that some characteristics of primitive melts can be preserved in evolved magmas.

CLV, in comparison to other MI, shows extreme enrichment in Th and Rb, creating a horizontal tendency in Fig. 5a, b that could be erroneously interpreted as related to fractional

crystallization. Such Th variation of ~20 ppm can only be reproduced after ~40% of fractional crystallization (considering a bulk partition coefficient for Th of 0.01), which is unreasonable given that CLV MI are hosted in Fo_{88-90} olivines. Therefore, the observed CLV trend must be explained by a process different to that of fractional crystallization.

In summary, we observe that MI and WR display different trends (Cotacachi-Cubilche, Puñalica, Sangay-Licto; Fig. 5) and that these differences cannot be related to a single fractional crystallization process. CLV MI and WR display a different behavior characterized by an extreme enrichment in Th and Rb. We propose that the positive-slope trends are related to partial melting processes, whereas the geochemical variation of CLV results of partial melting process of a heterogeneous mantle source characterized by an extreme enrichment of incompatible elements (Th, Rb).

5.2.2 Clues for CLV melt inclusion source given by alkali and volatile elements

Compositions of CLV MI are distinctively different from other Ecuadorian MI. We consider most MI to be classified as high-alumina basalts (HAB, Sisson and Grove, 1993) broadly within the calc-alkaline series because of their low K_2O, high Al_2O_3, and intermediate composition of CaO (Fig. 2b-d). The potential modifications of Fe, Mg, Si, and H concentrations due to PEM, would not alter this classification, as corrections are expected to be minor based on our test calculations (Fig. S3). However, CLV MI were clearly richer in K_2O and lower in Al_2O_3 (Fig. 2b-d). These differences suggest that different magma genesis mechanisms are present in the Ecuadorian arc system.

CLV MI, which are hosted in Fo_{88-90} olivines, were not (petrologically) related to HAB. In addition to lower Al_2O_3 and high K_2O concentrations, they were distinctively high in K_2O/Na_2O values (~1.9 while the other MI ~0.3; Table 4), which indicate a different source for CLV MI. In fact, K-rich lavas are common in the Ecuadorian arc and have been reported in volcanoes belonging to sub-Andean group (i.e., Sumaco volcano and Puyo cones), located to the south-east of CLV (Barragan et al., 1998; Hoffer et al., 2008). Based on the two following arguments, we concluded that a phlogopite- (phl-) lherzolite is the source of CLV. (1) The high K_2O/Na_2O values of CLV MI were comparable to those measured in small-degree (less than 5%) experimental melts of a phl-lherzolite in the garnet stability field (~3 GPa) reported by Condamine et al. (2016; K_2O ~6.4 wt.% and $(K_2O/Na_2O)<2$). (2) The high F (0.17-0.3 wt.%) measured in the MI indicated the presence of a mineral rich in F in the source. In fact, experimentally derived-melts of phl-bearing rocks can have F concentrations of between 0.3 to 0.5 wt.% (with phl and foiditic melts in equilibrium; Condamine et al., 2015). Fluorine concentration is controlled by the presence of phlogopite during mantle melting, similar to K_2O ($D_F^{(phl/m)}$~2, LaTourrette et al., 1995). Olivine-hosted MI from a phl-bearing mantle source show high F/Cl values of up to 5.1 (lava cones from Western Trans-Mexican Volcanic Belt, Vigouroux et al., 2008), while typical MI from continental arcs have F/Cl between values of 0.1-1 (Fig. 4). MI from CLV were the highest F/Cl (~5.2, Table 4) values reported so far in MI

for the Ecuadorian arc, and even higher than those reported by Vigouroux et al. (2008). This model of partial melting of a phl-lherzolite source for the K-rich CLV magmas agrees with that proposed for the rear-arc Conos de Puyo magmas (Hoffer et al., 2008).

5.3 Mantle and slab contributions, the constraints from trace elements systematics

5.3.1 Constraining the subducted sediment contribution and the mantle source composition

Plank (2005) showed that arc primitive basalts form linear "source" mixing arrays between mantle and sediment compositions in a diagram of Sm/La *vs.* Th/La. Following the approach, we have reproduced the diagram with Ecuadorian melt inclusion compositions and two sediment bulk compositions (Fig. 6a, b): (1) the newly analyzed compositions of sediments sampled along the Ecuadorian subduction trench and Manglares forearc basin; and (2) a siliceous nannofossil ooze of pelagic origin, sampled ~400 km off the coast of Ecuador during the deep sea drilling project (leg 62 site 504, Cann et al., 1983) which is also reported by Plank (2014). Before this work, the low Th/La (~0.08) of the sediments reported by Plank (2014) was used as an argument to state that Ecuadorian lavas with high Th/La (0.28-0.36) was acquired in the crust (Chiaradia et al, 2020). Here in the plot, the high Th/La of the newly analyzed sediments (up to 0.27) are higher than those of MI, suggesting that subducting sediments alone can impart the high Th/La of MI. The same conclusion can be reached from the diagram Th/La *vs.* Ba/Th (Fig. 6c) where MI plot between the composition of the two sediments and that of the mantle field represented by the composition of the Carnegie ridge basalts (Harpp et al., 2005). Because Ba (and Th) is a highly incompatible element, Ba/Th is expected to remain unchanged during mantle melting, and therefore the ratio measured in MI should be indicative of the melt sources, reflecting the composition of the slab component. Ba/Th is very low (~250) in the newly analyzed sediments but very high in that from Plank (2014). Geochemical variability of the Ecuadorian MI expressed on Fig. 6a-b can be explained by the involvement of two types of sediments into the mantle wedge. Thus, the crust contribution is unnecessary to explain the variation of Th/La and Ba/Th in primitive Ecuadorian MI. The distinction of two sediments based on Ba/Th has been recognized also in the Central American arc (Patino et al., 2000).

The whole rock field shown in Fig. 6 b-c correspond to rocks with variable silica content from the studied volcanoes (from 50 to 68 wt.% SiO_2). Some rocks that plot in this field (mainly those rich in silica, SiO_2>58 wt.%) have Th/La greater than the Th/La of the newly analyzed sediments. This geochemical signature can be acquired by processes occurring in the crust (i.e. crustal assimilation of high Th/La lithologies from Eastern Cordillera Fig. 6b) as proposed for some volcanoes in Ecuador (i.e. Chiaradia et al., 2020; Monzier et al., 1999). However, it is noteworthy to remember that the newly analyzed sediment samples correspond to terrigenous sediments of continental origin, and therefore its geochemical imprint is difficult to untangle from crustal contribution if the Th/La of crustal rocks is similar to that of the sediments. In any case, we based our reasoning in the following arguments to conclude that the slab component is

the main cause of the high Th/La of Ecuadorian MI and that the crust has a minor influence. Firstly, MI from CLV, with the highest Th/La are hosted in the most magnesian olivines (Fo_{88-90}) which indicates that the high Th/La is a feature of primitive magmas. Second, MI from Puñalica and Cubilche volcanoes have similar Th/La to MI from CLV, although they are constructed over different crustal rocks with contrasting Th/La. Puñalica and Cubilche are constructed over oceanic rocks from the Western Cordillera that depict low Th/La (Fig. 6d) while CLV is built over continental rocks from the Eastern Cordillera with high Th/La values (Litherland et al., 1994).

Figure 6 a-b also illustrates the potential presence of variable composition of the pre-metasomatised mantle because a mixing with a single mantle composition with sediments does not explain the entire variability. We have purposely plotted the composition of Sangay and Licto MI in a separate diagram because trace element systematics led us to conclude that the pre-metasomatized mantle below Sangay and Licto volcanoes was enriched. The principal characteristic that points towards an enriched pre-metasomatized mantle below the two volcanoes is their Nb-enrichment (represented by Nb/Nb* in Table 4) compared to other MI. Nb/Nb* in Licto and Sangay MI varies from 0.10 to 0.62, while in other MI, it varies from 0.03 to 0.10. Furthermore, Zr/Nb and Hf/Nb, which are low in OIB compared to MORB (Davidson, 1996; Dupuy et al., 1992) are also low in Sangay and Licto MI (Fig. 6e). Coming back to Fig. 6 a-b, the end-member mantle source for the Cotacachi, Cubilche, and Puñalica MI array intersects with the MORB region at a mid-point of Sm/La variation, indicating that the mantle source is mostly depleted (i.e., MORB-like), whereas the end-member mantle source for the Sangay and Licto (Fig. 6b) array is placed at a lower Sm/La, indicating an enriched mantle source with Sm/La values more similar to those of ocean island basalts (OIB).

Therefore, using the Plank (2005) trace elements systematics, we can demonstrate that the geochemical diversity of the Ecuadorian MI requires the involvement of two different sediment compositions. We also concluded that the mantle end-member for Licto and Sangay MI was more enriched, compared to the mantle end-member of MI from northern volcanoes and Puñalica.

5.3.2 Two types of slab components

The addition of incompatible elements via slab component to the mantle wedge gives arc magmas their archetypical trace element signature. The slab-related elements that enrich the mantle are referred to as non-conservative (Pearce and Peate, 1995). On the contrary, elements with no detectable slab contribution are referred to as conservative. Nb, for instance, can be considered analogous of conservative elements in Ecuadorian MI because they show the Nb negative anomaly when normalized to N-MORB with respect to La and Th (Fig. 3a-e). In Fig. 7a, MI are shown in a diagram of Nb/Yb *vs*. Th/Yb, and all MI plot above the MORB and OIB array, indicating that Th behaves as a non-conservative element (Pearce and Peate, 1995). The main characteristic that stands out in Fig. 7a is the two trends parallel to the MORB-OIB array,

one with high Th/Nb values (between 1.5 and 3) represented by MI from Puñalica and CLV, and the other with low Th/Nb (between 0.15 to 0.72) represented by MI from Cotacachi, Cubilche, Licto, and Sangay volcanoes (no data for Rucu Pichincha and PDA are available). Three Puñalica MI from one evolved lava (CAR83A, *cf.* Narváez et al. 2018) plot in the low Th/Nb trend unlike most MI from this volcano. The two trends of Fig. 7a, are also observed with other elements (e.g., with Ce, Nd as a numerator in the y-axis, Fig. S4). It should be noted that Fig. 7 is advantageous for deciphering the non-conservative slab inputs from non-conservative elements in a volcanic arc with different geochemical signals of mantle enrichment (or depletion) because both MORB (depleted mantle derived melt) and OIB (enriched mantle derived melt) plot along almost the same Th/Nb trend.

Fig. 7b shows that the fractional crystallization of two high-pressure mineral phases, able to fractionate Yb (hornblende and garnet), do not modify the Th/Nb value significantly and are unable to change the value from the low to the high Th/Nb trend. The assimilation-fractional crystallization (AFC) process was also unable to increase the Th/Nb from Cotacachi to CLV MI values. The assimilation of metamorphic rocks from the Eastern Cordillera (Th/Nb = 1.1, Litherland et al., 1994) using the DePaolo (1981) equation with a value of r=0.2, increases Th/Nb from 0.33 (mean value for Cotacachi MI) to 0.7 after 50% crystallization (bulk $D^{rock/magma}$ used for Th and Nb was 0.1 and 0.3, respectively, based on mineral partition coefficients from Green, 1994). Th/Nb values for Puñalica and CLV are even higher than 1.5; therefore, intracrustal processes (AFC or FC) cannot be the main process responsible for the high Th/Nb trend (Fig. 7). With these quantitative evaluations, we concluded that these two trends were due to a change in the metasomatic agent, one with low Th/Nb, and the other with high Th/Nb, added to the mantle wedge.

To identify the nature of the slab components, we compared trace element ratios that characterize the amount of material from the slab (Sr/Nb) to ratios indicative of its nature (B/Nb, La/Nb; either it is an aqueous fluid or a hydrous siliceous melt). Thus, two different trends were observed in a plot Sr/Nb *vs.* B/Nb (Fig. 8), in agreement with Th/Nb systematics. Because B is highly soluble in aqueous fluids (Leeman and Sisson, 1996), one trend rich in B/Nb (up to 22) corresponding to MI from Cotacachi, Cubilche (and to a lesser extent, Sangay and Licto) was considered to have a stronger "fluid" signature than those poor in B/Nb from CLV, Puñalica, and PDA (B/Nb: up to 4.4). Contrarily, in Fig. 8b, and given that La is an element preferentially partitioned into melts (Elliott et al., 1997), MI from CLV and Puñalica are considered to have a hydrous siliceous melt signature. PDA MI (orange filled circles) belong to the hydrous siliceous melt trend because of their lower B/Nb and higher La/Nb than the MI of the aqueous fluid trend, and because Le Voyer et al. (2008) concluded that their B isotopes signatures were correlated with this metasomatic agent. MI from Licto and Sangay clearly belong to the aqueous fluid trend in Fig. 8b but plot at low values of B/Nb in Fig. 8a because these MI have higher Nb than the MI of northern volcanoes (Nb/Nb*, Table 4) and Puñalica. The two trends observed in Fig. 8a, b are also seen when other fluid-immobile elements were used (i.e., Ce and Th; see Fig. S5).

Therefore, the Ecuadorian primitive MI demonstrate that the Ecuadorian sub-arc mantle was metasomatised by aqueous fluids and (or) hydrous siliceous melts. This change of the nature

of the slab flux implies a variation of physical conditions at the slab surface, as dehydration reactions occur at lower temperature conditions than melting reactions (Kessel et al., 2005).

5.3.3 Geochemical modelling of primitive melt inclusions

In the present section, we modelled the magma genesis of primitive Ecuadorian arc magmas using representative MI from each studied volcano following three successive steps. First, we calculated the composition of the slab component using Arc Basalt Simulator 3 spreadsheet (ABS; Kimura et al., 2010). Second, we used a bulk mixing equation to mix the slab component with the peridotite composition, and lastly we melted the metasomatised mantle source using a batch melting equation. We considered the following geochemical constraints established in previous sections. First, the slab component for CLV, Puñalica, and PDA was set as a hydrous siliceous melt, while for the others, it was an aqueous fluid (section 5.3.2). Second, the mantle composition was considered as enriched for Puñalica and Sangay volcanoes compared to other volcanoes (section 5.3.1).

ABS tracks the residual mineral proportion during mantle melting and the mineral proportion during dehydration or melting of altered oceanic crust and sediment, following the information determined by pMELTS and Perple_X simulations for different mantle, altered basaltic oceanic crust (AOC), and terrigenous sediment (SED) compositions. The equilibrium mineral assemblages for the AOC and SED were calculated at 3.6 GPa (~120 km) for CLV, Puñalica, Licto, and Sangay, and 2.5 GPa (~80 km) for Cotacachi and Cubilche, roughly corresponding to the pressure at the surface of the subducted slab under each volcano (Fig. 1). The temperature of the slab surface was taken from the P-T trajectories determined by Syracuse et al. (2010) model for the Colombia/Ecuador subduction zone (911°C at 3.6 GPa, and 780°C at 2.5 GPa), where the oceanic crust is young (i.e. 15 Ma) and correspond to the subduction segment north of GFZ. Under such P-T conditions, Perplex_X simulations included in ABS, calculated that the subducting slab dehydrates at depths of the Cotacachi and Cubilche locations, and it melts beneath CLV and Puñalica. For the subduction segment south of GFZ, where the subducted oceanic crust is older (i.e. >30 Ma) compared to the north of GFZ, no thermal model exists. However, from the work of Syracuse et al. (2010), we conclude that the subduction of older oceanic crust should render lower temperatures at a given pressure along the subduction zone. Therefore, the slab surface temperature below Licto and Sangay volcanoes should be lower to that obtained beneath CLV and Puñalica, that are located at similar distance to the slab (Fig. 1b). This is consistent with the conclusion reached in section 5.3.3 where we identified that the slab component under Licto and Sangay volcanoes was an aqueous fluid, which correspond to a lower temperature. Therefore, we ran the ABS calculations with a temperature lower by 40°C for these two volcanoes, thus fullfilling the subsolidus condition of altered oceanic crust and sediments.

Having defined the degree of melting or dehydration and the mineral proportion of the residue for each reservoir (i.e., AOC, SED), ABS calculates the partition coefficient ($D_a^{\text{mineral/(melt,fluid)}}$) between fluid (or melt) and minerals. ABS uses T-dependent partition

coefficients for garnet and clinopyroxene (Kessel et al., 2005); fixed partition coefficient for lawsonite, chloritoid, phengite, zoisite, lawsonite, olivine and rutile (several authors; *cf.* Kimura et al., 2010); and for other minerals the partition coefficients are obtained by extrapolation of $D^{mineral/mineral}$ using natural rocks. For partition coefficients for mantle melting, ABS uses the values of Green et al. (2000). In addition, in supplementary material Fig. S6, we compare the partition coefficients calculated with ABS at the conditions of interest for AOC with those of Kessel et al. (2005) and Rustioni et al. (2019) to show that ABS returned partition coefficients that are expected in subduction zones. For AOC and SED, we used the mean basalt composition from the Carnegie ridge (Harpp et al., 2005) and that of the newly analyzed sediments on the Ecuadorian subduction system (Table 2), respectively. No carbonates were used as the sediment composition because carbonates have not been sampled in front of the subduction trench. For Licto and Sangay, we used a primitive mantle composition (Sun and McDonough, 1989) –with an extraction of 1% of MORB– and that of a depleted mantle composition (Workman and Hart, 2005) for all the other volcanoes. These compositions therefore accounted for the heterogeneity of the subarc mantle (Fig. 6e). Finally, we used a batch melting equation for mantle melting considering an arbitrary melting degree of 5% (or 10%), and an initial composition resulting from mixing between the slab component and the mantle. For each simulation, we added an amount of slab component until we obtained a good fit between the natural and the modelled compositions (Fig. 9a for CLV and Cotacachi and Fig. S7 for other volcanoes, see Table 5 for modeling details).

Fig. 9b shows the composition of the aqueous fluid component calculated by ABS for Cotacachi to illustrate the effect of adding different proportions of this component into the mantle wedge in the Nb/Yb *vs.* Th/Yb space. Because the figure is a ratio-ratio plot, an addition of fluid significantly offsets the initial Th/Nb values from the OIB-MORB trend, although a fluid is known as less effective metasomatic agent compared to a melt. Also, the figure shows the effect of the abundance of garnet in the mantle residue. Fig. 9c displays in the same diagram Nb/Yb *vs.* Th/Yb, the results of modeling for varying degrees of mantle melting and mantle compositions. From Fig. 9b-c, we concluded that the magma compositions of the low Th/Nb array were reproducible with combinations of the following parameters with an aqueous fluid input from the slab: vol.% of garnet left in the residue (dotted lines in Fig. 9b, causing large variation of Th/Nb), percentage of slab component added (solid lines in Fig. 9b, causing variation along a constant Th/Nb), degree of mantle melting (Fig. 9c, variation to low Th and Nb with constant Th/Nb), and mantle composition (Fig. 9c, variation to high Th and Nb with mantle enrichment, constant Th/Nb).

The change in Th/Nb due to melting of an aqueous fluid-metasomatised mantle is insufficient to reproduce the magma compositions of CLV and Puñalica (Fig. 9b, c). No combination of parameters resulted in an observed Th increase over Nb. An obvious alternative explanation was the change in the nature of the slab component to a silicate melt, instead of an aqueous fluid. In fact, the presence of the slab melt beneath CLV and Puñalica was expected from the PT condition (Syracuse et al., 2010) and trace element systematics (section 5.3.2). ABS simulations therefore provide a test that examines the full spectrum of trace elements with this scenario. According to Kimura et al. (2010), ABS calculates the slab melt with a set of D_a that

are different from those of aqueous fluid by a factor of 2 to 10, similar to the values reported by Moyen and Stevens (2006) for amphibolite melting. The results of this calculation are shown in Fig. 9d (solid line), where CLV and Puñalica magmas are reproduced with 5% mantle melting after the addition of 5 to 20 wt.% of a hydrous siliceous melt. Also shown in Fig. 9d are the results of the phlogopite-lherzolite melting model developed to explain the CLV primitive magma diversity (see section 5.2.2). For this, we used phlogopite partition coefficients from Halliday et al. (1995), and we assigned 7% residual phlogopite to the mantle, which is similar to the values reported by Condamine et al. (2016) for phlogopite-lherzolite melting experiments at 3 GPa. In summary, the high Th/Nb array is only attainable by adding a hydrous siliceous melt to the mantle wedge given that a siliceous melt component is enriched in most trace elements compared to an aqueous fluid component.

5.4 Geochemical signatures of melt inclusions in the geodynamic context of Ecuadorian continental arc

The across-arc geochemical variations are conventionally explained by compositional changes of slab component due to continuous devolatilization during slab subduction, which in turn controls the extent of partial melting of the mantle (e.g., Tatsumi, 1986). In their pioneering work on the Ecuadorian arc, Barragan et al. (1998) interpreted that the amount of fluids added to the mantle wedge decreases from west to east resulting in a high LILE over HFSE or LREE ratios (e.g., Ba/La, Ba/Nb) in volcanoes of the frontal arc (i.e., Atacazo volcano), and low ratios in those from the sub-Andean group in the east (i.e. Sumaco volcano). In general, MI show similar tendency to whole-rocks (Fig. 10a-c): Cotacachi and Rucu Pichincha being among the volcanoes with the highest LILE over HFSE or LREE ratios, and PDA showing the lowest values. The results of this study confirm the variations of slab component across the arc.

More recently, Ancellin et al. (2017) and Chiaradia et al. (2020) recognized a north-south (along-arc) geochemical zonation among the lavas from the frontal arc. Both studies show that Ba/Th was maximum around the equator and decreases towards the north and south. Ancellin et al. (2017) proposed that such geochemical zonation is due to a change in the slab component composition, while Chiaradia et al. (2020), who also reported a north-south variation of other elements (i.e., Nd, Sm, Nb), argue that it is due to magma-crust interactions at a distinctive depth. Our data are unable to confirm the origin of this geochemical zonation reported in volcanoes from the frontal arc, as Cotacachi and Rucu Pichincha volcanoes are the only front-arc volcanoes in this study, and Th concentration data is not available for Rucu Pichincha MI. However, we found an along-arc variability of trace elements in MI from volcanoes that are located at approximately 120 km above the subducting slab (i.e., CLV, Puñalica, Licto, and Sangay). CLV and Puñalica MI are relatively enriched in fluid-immobile elements (high La/Nb, Th/Nb), while Licto and Sangay MI show a preference for fluid-mobile elements (high Ba/La, Pb/Ce, and B/Nb). We concluded that such variation was due to a change in the slab component composition. Such systematics are therefore consistent with the interpretation of Ancellin et al. (2017). We stress that these previous studies reported whole-rock geochemical data, and it would have been difficult to separate geochemical signals from crustal or slab components.

To account for the change in the slab component along the Ecuadorian arc, we propose that the thermal regime along the subduction zone is hotter to the north of GFZ compared to the south. Thus, a higher temperature at a given pressure would allow the slab to melt and produce the hydrous siliceous melt component under CLV, Puñalica, and PDA volcanoes. We consider that the age difference of the oceanic crust in the north and south of the GFZ is the main cause that controls the thermal regime. North of the GFZ, the oceanic crust is younger (12-20 Ma) than to the south (25-30 Ma, Yepes et al., 2016). In this model, the location of the GFZ under the Ecuadorian arc is a crucial dividing line of the arc thermal regime and thus slab geochemical components. It should be noted that the prolongation of GFZ into the volcanic arc was identified under Puñalica volcano based on an anomalous chlorine enrichment of Puñalica MI (Fig. 4; Narváez et al., 2018). Greater interactions between the oceanic water and the oceanic crust along the fracture zone was attributed as the cause of Cl enrichment and imparts its signature to Puñalica MI. In conclusion, we interpret that the subducting slab to the north of Puñalica introduces greater thermal energy into the sub-arc zone than to the south, and this difference in the subducted slab thermal regime produces the along-arc geochemical variations.

The high Cl content and low F/Cl (0.14 ± 0.02) of Puñalica MI are indicative of the GFZ location under Puñalica volcano. On the contrary, other Ecuadorian MI with aqueous fluid signatures have a F/Cl value of around ~0.43±0.07 that is independent of the depth to the Benioff zone (i.e., Cotacachi, Cubilche, Licto, Sangay, and Rucu Pichincha, Fig. 10d), making it a contrasting geochemical signature from Ba/Nb and Ba/La, which negatively correlated with the Benioff zone depth, probably related to the amount of fluids released. We speculate that the almost constant F/Cl value represents the composition of the aqueous fluids released during metamorphic dehydration reactions occurring in the subducting slab and provides a reference value to identify the involvement of fluid in its source. A constant F/Cl value is possible if the fluid composition is buffered by the mineral assemblage during dehydration reactions. Finally, we consider that the F/Cl of CLV (5.2±1.7), PDA (0.83±0.24), and Sangay-SAN20B (0.42±0.05) do not represent that of the fluids or melts coming from the subducting slab, as the mantle source of these MI was in equilibrium either with phlogopite (CLV) or hornblende (PDA, Le Voyer et al., 2008; SAN20B, Narváez et al., 2018) capable of fractionating F/Cl.

In a previous section, we argued that the low Zr/Nb and Hf/Nb in Sangay and Licto MI (Fig. 6d) were indicative of a mantle enrichment under those volcanoes. The southern location of Sangay and Licto volcanoes led us to think that there was an along-arc variation of composition of the sub-arc mantle. However, the presence of geochemical heterogeneity of the Ecuadorian sub-arc mantle is less clear when whole-rock data are examined. For example, primitive whole rocks (Mg#>55, using Ancellin et al. 2017 database) from volcanoes located in the north, and some from the sub-Andean zone, also show low Zr/Nb values (Hf is not available for whole-rocks). Therefore, we conclude that low Zr/Nb (and most probably low Hf/Nb) is not only a feature of southern volcanoes, and that local heterogeneities of the sub-arc mantle may occur all along the Ecuadorian arc. We note that Chiaradia et al. (2020) proposed that the variability of Nb in volcanoes from the frontal arc was related to variable rutile fractionation in the crust. This explanation can be applied to silicic hydrous magma in which rutile can be saturated at several hundred ppm of TiO_2 (Gaetani et al., 2008). However, it would not apply to

the primitive basalt study presented here. Rutile saturation in basalt requires several wt.% of TiO_2 (Ryerson and Watson, 1987). Based on these studies, the Nb variations in our primitive MI cannot be derived from rutile crystallization or from dissolution in the crust but rather represent the variable composition of the parental magmas.

6 Conclusions

In order to decipher the slab components that metasomatise the sub-arc mantle, we studied 83 olivine-hosted MI that represent the most primitive melts from the Ecuadorian arc. Together with the dataset published by Le Voyer et al. (2008) and Narváez et al. (2018) from other Ecuadorian volcanoes, we identified two types of slab components. On the basis of a systematic trace element analysis, we identified a slab component that is rich in fluid-mobile elements (Ba/La: 30-110 and Pb/Ce: 0.1-0.5, B/Nb: up to 22) and poor in fluid-immobile elements (La/Nb: 2.2-4, Th/Nb: up to 0.7), indicating an aqueous fluid. The second slab component that is relatively enriched in fluid-immobile elements (La/Nb:7.2-15.5, Th/Nb: up to 3.2), and has low contents of fluid-mobile elements (Ba/La: 15-36, Pb/Ce: 0.02-0.1, B/Nb: up to 4.4) is indicative of a hydrous siliceous melt. We distinguished the aqueous fluid signature in most MI, except for those coming from CLV, Puñalica, and PDA volcanoes. In addition to this systematics, almost all MI with an aqueous fluid-like signature show a similar F/Cl value of around 0.43 ± 0.07, potentially indicating the aqueous fluid component in the Ecuadorian arc.

The geographical limit separating the production of aqueous fluids and hydrous siliceous melts at the surface of the slab depends on the location of the GFZ, which is below Puñalica volcano. This oceanic structure separates a young and probably hotter oceanic crust to the north from an older and likely colder oceanic crust to the south. Thus, the hotter thermal regime to the north of the GFZ would allow the subducting slab to melt.

We also showed that Ecuadorian MI compositions are indicative of the mantle composition and mineral stability in the sub-arc mantle. For instance, we correlated the high Nb/Nb* and low Zr/Nb, Hf/Nb, Sm/La of Conos de Licto and Sangay MI with the melting of an enriched mantle. Such enrichment is not correlated with the slab component addition and shows that the sub-arc mantle is heterogeneous under the Ecuadorian arc. Finally, we consider that the high K_2O/Na_2O (~1.9) and F/Cl (5.2±1.7) are indicative of the phlogopite stability in the mantle source of CLV MI.

This MI study of Ecuadorian volcanoes achieved the identifications of primitive magmas in each of the studied volcanoes. With minimum influence from crustal modifications, these data illustrated the variation of thermal state below the arc crust and furthermore identified the location of the geographical divide between hot and cold regimes. In addition, we reported potential indications of mantle heterogeneity below the arc. Presence of slab melting was geochemically identified, as well as the involvement of phlogopite and amphibole as a residual phase during mantle melting.

Declaration of Competing Interest

The authors declare that they have no known competing financial interests or personal relationships that could have appeared to influence the work reported in this paper.

Acknowledgments

This work is part of an Ecuadorian-French cooperation program conducted between the Instituto Geofísico of the Escuela Politécnica Nacional (IG-EPN) and the Institut de Recherche pour le Développement (IRD, France), through the joint laboratory project “Seismes et Volcans dans les Andes du Nord (SVAN)”. This research was partly financed by the French Government Laboratory of Excellence initiative N° ANR-10-LABX-0006, the Auvergne Region and the European Regional Development Fund. This is Laboratory of Excellence ClerVolc contribution number ##. DN thanks IRD for financial support of his PhD through the ARTS scholarship. Extended.

Data availability

Table 3 is freely available in the EarthChem library (https://doi.org/10.26022/IEDA/111625) upon acceptance of the paper.

References

Allègre, C. J., & Minster, J. F. (1978). Quantitative models of trace element behavior in magmatic processes. Earth and Planetary Science Letters, 38(1), 1–25. https://doi.org/10.1016/0012-821X(78)90123-1

Almeida, M. (2016). Estudio petrográfico y geoquímico del volcán Cotacachi – provincia de Imbabura (Ingeniero Geólogo). Escuela Politécnica Nacional, Ecuador.

Ancellin, M.-A., Samaniego, P., Vlastélic, I., Nauret, F., Gannoun, A., & Hidalgo, S. (2017). Across-arc versus along-arc Sr-Nd-Pb isotope variations in the Ecuadorian volcanic arc. Geochemistry, Geophysics, Geosystems. https://doi.org/10.1002/2016GC006679

Bablon, M., Quidelleur, X., Samaniego, P., Le Pennec, J.-L., Audin, L., Jomard, H., et al. (2019). Interactions between volcanism and geodynamics in the southern termination of the Ecuadorian arc. Tectonophysics, 751, 54–72. https://doi.org/10.1016/j.tecto.2018.12.010

Bablon, M., Quidelleur, X., Samaniego, P., Le Pennec, J.-L., Santamaría, S., Liorzou, C., et al. (2020). Volcanic history reconstruction in northern Ecuador: insights for eruptive and erosion rates on the whole Ecuadorian arc. Bulletin of Volcanology, 82(1), 11. https://doi.org/10.1007/s00445-019-1346-1

Barragan, R., Geist, D., Hall, M., Larson, P., & Kurz, M. (1998). Subduction controls on the compositions of lavas from the Ecuadorian Andes. Earth and Planetary Science Letters, 154(1–4), 153–166. https://doi.org/10.1016/S0012-821X(97)00141-6

Bryant, J. A., Yogodzinski, G. M., Hall, M. L., Lewicki, J. L., & Bailey, D. G. (2006). Geochemical constraints on the origin of volcanic rocks from the Andean northern volcanic zone, Ecuador. Journal of Petrology, 47(6), 1147–1175. https://doi.org/10.1093/petrology/egl006

Bucholz, C. E., Gaetani, G. A., Behn, M. D., & Shimizu, N. (2013). Post-entrapment modification of volatiles and oxygen fugacity in olivine-hosted melt inclusions. Earth and Planetary Science Letters, 374, 145–155. https://doi.org/10.1016/j.epsl.2013.05.033

Cann, J. R., Langseth, M. G., Honnorez, J., Von Herzen, R. P., & White, S. M. (1983). Sites 501 and 504: sediments and ocean crust in an area of high heat flow on the southern flank of the Costa Rica rift. In Initials reports of the Deep Sea Drilling Project, leg 69. Washington: U.S. Govt. Printing office.

Carter, L. B., Skora, S., Blundy, J. D., De Hoog, J. C. M., & Elliott, T. (2015). An experimental study of trace element fluxes from subducted oceanic crust. Journal of Petrology, 56(8), 1585–1606. https://doi.org/10.1093/petrology/egv046

Chaussidon, M., & Marty, B. (1995). Primitive boron isotope composition of the mantle. Science, 269(5222), 383–386. https://doi.org/10.1126/science.269.5222.383

Cherniak, D. J. (2010). REE diffusion in olivine. American Mineralogist, 95(2–3), 362–368. https://doi.org/10.2138/am.2010.3345

Chiaradia, M., Müntener, O., & Beate, B. (2020). Effects of aseismic ridge subduction on the geochemistry of frontal arc magmas. Earth and Planetary Science Letters, 531, 115984. https://doi.org/10.1016/j.epsl.2019.115984

Collot, J.-Y., Ratzov, G., Silva, P., Proust, J. -N., Migeon, S., Hernandez, M. -J., et al. (2019). The Esmeraldas canyon: A helpful marker of the Pliocene-Pleistocene tectonic deformation of the north Ecuador-southwest Colombia convergent margin. Tectonics, 2019TC005501. https://doi.org/10.1029/2019TC005501

Condamine, P. (2015). Rôle du phlogopite sur la genèse de magmas riches en potassium : Approche expérimentale (Doctoral Thesis). Université Blaise Pascal - Clermont-Ferrand II, France.

Condamine, P., Médard, E., & Devidal, J.-L. (2016). Experimental melting of phlogopite-peridotite in the garnet stability field. Contributions to Mineralogy and Petrology, 171(11), 95. https://doi.org/10.1007/s00410-016-1306-0

Cotten, J., Le Dez, A., Bau, M., Caroff, M., Maury, R. C., Dulski, P., et al. (1995). Origin of anomalous rare-earth element and yttrium enrichments in subaerially exposed basalts: Evidence from French Polynesia. Chemical Geology, 119(1), 115–138. https://doi.org/10.1016/0009-2541(94)00102-E

Danyushevsky, L. V., Della-Pasqua, F. N., & Sokolov, S. (2000). Re-equilibration of melt inclusions trapped by magnesian olivine phenocrysts from subduction-related magmas: petrological implications. Contributions to Mineralogy and Petrology, 138(1), 68–83. https://doi.org/10.1007/PL00007664

Davidson, J. P. (1996). Deciphering mantle and crustal signatures in subduction zone magmatism. In Subduction: top to bottom (pp. 251–262). American Geophysical Union (AGU). https://doi.org/10.1029/GM096p0251

DePaolo, D. J. (1981). Trace element and isotopic effects of combined wallrock assimilation and fractional crystallization. Earth and Planetary Science Letters, 53(2), 189–202. https://doi.org/10.1016/0012-821X(81)90153-9

Dupuy, C., Liotard, J. M., & Dostal, J. (1992). Zr/Hf fractionation in intraplate basaltic rocks: carbonate metasomatism in the mantle source. Geochimica et Cosmochimica Acta, 56(6), 2417–2423. https://doi.org/10.1016/0016-7037(92)90198-R

Elliot, T., Plank, T., Zindler, A., White, W., & Bourdon, B. (1997). Element transport from slab to volcanic front at the Mariana arc. Journal of Geophysical Research: Solid Earth, 102(B7), 14991–15019. https://doi.org/10.1029/97JB00788

Ford, C. E., Russell, D. G., Craven, J. A., & Fisk, M. R. (1983). Olivine-liquid equilibria: Temperature, pressure and composition dependence of the crystal/liquid cation partition coefficients for Mg, Fe 2+, Ca and Mn. Journal of Petrology, 24(3), 256–266. https://doi.org/10.1093/petrology/24.3.256

Gaetani, G. A., Asimow, P. D., & Stolper, E. M. (2008). A model for rutile saturation in silicate melts with applications to eclogite partial melting in subduction zones and mantle plumes. Earth and Planetary Science Letters, 272(3–4), 720–729. https://doi.org/10.1016/j.epsl.2008.06.002

Green, T. H. (1994). Experimental studies of trace-element partitioning applicable to igneous petrogenesis—Sedona 16 years later. Chemical Geology, 117(1–4), 1–36.

Green, T. H., Blundy, J. D., Adam, J., & Yaxley, G. M. (2000). SIMS determination of trace element partition coefficients between garnet, clinopyroxene and hydrous basaltic liquids at 2–7.5 GPa and 1080–1200°C. Lithos, 53(3–4), 165–187. https://doi.org/10.1016/S0024-4937(00)00023-2

Hall, M. L., Samaniego, P., Le Pennec, J. L., & Johnson, J. B. (2008). Ecuadorian Andes volcanism: A review of Late Pliocene to present activity. Journal of Volcanology and Geothermal Research, 176(1), 1–6. https://doi.org/10.1016/j.jvolgeores.2008.06.012

Halliday, A. N., Lee, D.-C., Tommasini, S., Davies, G. R., Paslick, C. R., Godfrey Fitton, J., & James, D. E. (1995). Incompatible trace elements in OIB and MORB and source enrichment in the sub-oceanic mantle. Earth and Planetary Science Letters, 133(3), 379–395. https://doi.org/10.1016/0012-821X(95)00097-V

Harpp, K. S., Wanless, V. D., Otto, R. H., Hoernle, K., & Werner, R. (2005). The Cocos and Carnegie aseismic ridges: a trace element record of long-term plume–spreading center interaction. Journal of Petrology, 46(1), 109–133. https://doi.org/10.1093/petrology/egh064

Hauri, E. (2002). SIMS analysis of volatiles in silicate glasses, 2: isotopes and abundances in Hawaiian melt inclusions. Chemical Geology, 183(1), 115–141. https://doi.org/10.1016/S0009-2541(01)00374-6

Hermann, J., & Rubatto, D. (2009). Accessory phase control on the trace element signature of sediment melts in subduction zones. Chemical Geology, 265(3–4), 512–526. https://doi.org/10.1016/j.chemgeo.2009.05.018

Hidalgo, S., Gerbe, M. C., Martin, H., Samaniego, P., & Bourdon, E. (2012). Role of crustal and slab components in the Northern Volcanic Zone of the Andes (Ecuador) constrained by Sr–Nd–O isotopes. Lithos, 132–133, 180–192. https://doi.org/10.1016/j.lithos.2011.11.019

Hoffer, G., Eissen, J.-P., Beate, B., Bourdon, E., Fornari, M., & Cotten, J. (2008). Geochemical and petrological constraints on rear-arc magma genesis processes in Ecuador: The Puyo cones and Mera lavas volcanic formations. Journal of Volcanology and Geothermal Research, 176(1), 107–118. https://doi.org/10.1016/j.jvolgeores.2008.05.023

Kerr, A. C., Aspden, J. A., Tarney, J., & Pilatasig, L. F. (2002). The nature and provenance of accreted oceanic terranes in western Ecuador: geochemical and tectonic constraints. Journal of the Geological Society, 159(5), 577–594.

Kessel, R., Schmidt, M. W., Ulmer, P., & Pettke, T. (2005). Trace element signature of subduction-zone fluids, melts and supercritical liquids at 120–180 km depth. Nature, 437(7059), 724–727. https://doi.org/10.1038/nature03971

Kimura, J.-I., Kent, A. J. R., Rowe, M. C., Katakuse, M., Nakano, F., Hacker, B. R., et al. (2010). Origin of cross-chain geochemical variation in Quaternary lavas from the northern Izu arc: using a quantitative mass balance approach to identify mantle sources and mantle wedge processes. Geochemistry, Geophysics, Geosystems, 11(10), 24. https://doi.org/10.1029/2010GC003050

Koch, C. D., Delph, J., Beck, S. L., Lynner, C., Ruiz, M., Hernandez, S., et al. (2021). Crustal thickness and magma storage beneath the Ecuadorian arc. Journal of South American Earth Sciences, 110, 103331. https://doi.org/10.1016/j.jsames.2021.103331

LaTourrette, T., Hervig, R. L., & Holloway, J. R. (1995). Trace element partitioning between amphibole, phlogopite, and basanite melt. Earth and Planetary Science Letters, 135(1), 13–30. https://doi.org/10.1016/0012-821X(95)00146-4

Le Bas, M. J., Le Maitre, R. W., Streckeisen, A., Zanettin, B., & others. (1986). A chemical classification of volcanic rocks based on the total alkali-silica diagram. Journal of Petrology, 27(3), 745–750.

Le Voyer, M. (2009). Rôle des fluides dans la genèse des magmas d'arcs : analyses in situ des éléments volatils et des isotopes du bore dans les inclusions magmatiques des olivines primitives (Doctoral Thesis). Université Blaise Pascal - Clermont-Ferrand II, France.

Le Voyer, M., Rose-Koga, E. F., Laubier, M., & Schiano, P. (2008). Petrogenesis of arc lavas from the Rucu Pichincha and Pan de Azúcar volcanoes (Ecuadorian arc): major, trace element, and boron isotope evidences from olivine-hosted melt inclusions. Geochemistry, Geophysics, Geosystems, 9(12), 27. https://doi.org/10.1029/2008GC002173

Leeman, W. P., & Sisson, V. B. (1996). Geochemistry of boron and its implications for crustal and mantle processes. Reviews in Mineralogy and Geochemistry, 33(1), 645–707.
Leroux, P., Shirey, S., Hauri, E., Perfit, M., & Bender, J. (2006). The effects of variable sources, processes and contaminants on the composition of northern EPR MORB (8–10°N and 12–14°N): evidence from volatiles (H2O, CO2, S) and halogens (F, Cl). Earth and Planetary Science Letters, 251(3–4), 209–231. https://doi.org/10.1016/j.epsl.2006.09.012
Litherland, M., Aspen, J. A., & Jemielita, R. A. (1994). The metamorphic belts of Ecuador. British Geological Survey.
McDonough, W. F., & Sun, S. S. (1995). The composition of the Earth. Chemical Geology, 120(3), 223–253. https://doi.org/10.1016/0009-2541(94)00140-4
Monzier, M., Robin, C., Samaniego, P., Hall, M. L., Cotten, J., Mothes, P., & Arnaud, N. (1999). Sangay volcano, Ecuador: structural development, present activity and petrology. Journal of Volcanology and Geothermal Research, 90(1–2), 49–79. https://doi.org/10.1016/S0377-0273(99)00021-9
Moyen, J.-F., & Stevens, G. (2006). Experimental constraints on TTG petrogenesis: implications for Archean geodynamics. In K. Benn, J.-C. Mareschal, & K. C. Condie (Eds.), Geophysical Monograph Series (Vol. 164, pp. 149–175). Washington, D. C.: American Geophysical Union. https://doi.org/10.1029/164GM11
Narváez, D. F., Rose-Koga, E. F., Samaniego, P., Koga, K. T., & Hidalgo, S. (2018). Constraining magma sources using primitive olivine-hosted melt inclusions from Puñalica and Sangay volcanoes (Ecuador). Contributions to Mineralogy and Petrology, 173(10), 80. https://doi.org/10.1007/s00410-018-1508-8
Navarrete, W. F., Le Pennec, J. L., Solano, S., Liorzou, C., & Ruiz, G. A. (2020). A first reconstruction of the evolution of Cubilche Volcanic Complex, Imbabura Province, Ecuador. Journal of Volcanology and Geothermal Research, 406, 107023. https://doi.org/10.1016/j.jvolgeores.2020.107023
Nocquet, J.-M., Villegas-Lanza, J. C., Chlieh, M., Mothes, P. A., Rolandone, F., Jarrin, P., et al. (2014). Motion of continental slivers and creeping subduction in the northern Andes. Nat. Geosci, 7(4), 287–291.
Patino, L. C., Carr, M. J., & Feigenson, M. D. (2000). Local and regional variations in Central American arc lavas controlled by variations in subducted sediment input. Contributions to Mineralogy and Petrology, 138(3), 265–283. https://doi.org/10.1007/s004100050562
Pearce, J. A., & Peate, D. W. (1995). Tectonic implications of the composition of volcanic arc magmas. Annual Review of Earth and Planetary Sciences, 23(1), 251–285.
Peccerillo, A., & Taylor, S. R. (1976). Geochemistry of Eocene calc-alkaline volcanic rocks from the Kastamonu area, northern Turkey. Contributions to Mineralogy and Petrology, 58(1), 63–81.
Plank, T. (2005). Constraints from thorium/lanthanum on sediment recycling at subduction zones and the evolution of the continents. Journal of Petrology, 46(5), 921–944. https://doi.org/10.1093/petrology/egi005
Plank, T. (2014). The Chemical Composition of Subducting Sediments. In Treatise on Geochemistry (pp. 607–629). Elsevier.
Portnyagin, M., Mironov, N., Botcharnikov, R., Gurenko, A., Almeev, R. R., Luft, C., & Holtz, F. (2019). Dehydration of melt inclusions in olivine and implications for the origin of silica-undersaturated island-arc melts. Earth and Planetary Science Letters, 517, 95–105. https://doi.org/10.1016/j.epsl.2019.04.021
Ratzov, G., Collot, J.-Y., Sosson, M., & Migeon, S. (2010). Mass-transport deposits in the Northern Ecuador subduction trench: Result of frontal erosion over multiple seismic cycles. Earth and Planetary Science Letters, 296(1–2), 89–102. https://doi.org/10.1016/j.epsl.2010.04.048
Robin, C., Samaniego, P., Pennec, J.-L. L., Fornari, M., & Mothes, P. (2010). New radiometric and petrological constraints on the evolution of the Pichincha volcanic complex (Ecuador). Bulletin of Volcanology, 72, 21. https://doi.org/10.1007/s00445-010-0389-0
Rogers, G., & Hawkesworth, C. J. (1989). A geochemical traverse across the North Chilean Andes: evidence for crust generation from the mantle wedge. Earth and Planetary Science Letters, 91(3), 271–285. https://doi.org/10.1016/0012-821X(89)90003-4
Rose-Koga, E. F., Koga, K. T., Hamada, M., Hélouis, T., Whitehouse, M. J., & Shimizu, N. (2014). Volatile (F and Cl) concentrations in Iwate olivine-hosted melt inclusions indicating low-temperature subduction. Earth, Planets and Space, 66(1), 1–12.
Rustioni, G., Audétat, A., & Keppler, H. (2019). Experimental evidence for fluid-induced melting in subduction zones. Geochemical Perspectives Letters, 49–54. https://doi.org/10.7185/geochemlet.1925
Ryerson, F. J., & Watson, E. B. (1987). Rutile saturation in magmas: implications for Ti-Nb-Ta depletion in island-arc basalts. Earth and Planetary Science Letters, 86(2), 225–239. https://doi.org/10.1016/0012-821X(87)90223-8
Samaniego, P., Martin, H., Monzier, M., Robin, C., Fornari, M., Eissen, J.-P., & Cotten, J. (2005). Temporal evolution of magmatism in the northern volcanic zone of the Andes: the geology and petrology of Cayambe Volcanic Complex (Ecuador). Journal of Petrology, 46(11), 2225–2252. https://doi.org/10.1093/petrology/egi053

Shaw, A. M., Behn, M. D., Humphris, S. E., Sohn, R. A., & Gregg, P. M. (2010). Deep pooling of low degree melts and volatile fluxes at the 85°E segment of the Gakkel Ridge: Evidence from olivine-hosted melt inclusions and glasses. Earth and Planetary Science Letters, 289(3–4), 311–322. https://doi.org/10.1016/j.epsl.2009.11.018

Sisson, T. W., & Grove, T. L. (1993). Experimental investigations of the role of H2O in calc-alkaline differentiation and subduction zone magmatism. Contributions to Mineralogy and Petrology, 113(2), 143–166. https://doi.org/10.1007/BF00283225

Sobolev, A. V., Dmitriev, L. V., Barsukov, V. L., Nevsorov, V. N., & Slutskii, A. B. (1980). The formation conditions of the high-magnesium olivines from the monomineralic fraction of Luna 24 regolith. In Lunar and Planetary Science Conference Proceedings (Vol. 11, pp. 105–116).

Sorbadere, F., Schiano, P., Métrich, N., & Bertagnini, A. (2013). Small-scale coexistence of island-arc- and enriched-MORB-type basalts in the central Vanuatu arc. Contributions to Mineralogy and Petrology, 166(5), 1305–1321. https://doi.org/10.1007/s00410-013-0928-8

Spandler, C., Mavrogenes, J., & Hermann, J. (2007). Experimental constraints on element mobility from subducted sediments using high-P synthetic fluid/melt inclusions. Chemical Geology, 22.

Spilliaert, N., Metrich, N., & Allard, P. (2006). S–Cl–F degassing pattern of water-rich alkali basalt: Modelling and relationship with eruption styles on Mount Etna volcano. Earth and Planetary Science Letters, 248(3–4), 772–786. https://doi.org/10.1016/j.epsl.2006.06.031

Streck, M. J., Leeman, W. P., & Chesley, J. (2007). High-magnesian andesite from Mount Shasta: A product of magma mixing and contamination, not a primitive mantle melt. Geology, 35(4), 351–354.

Sun, S. S., & McDonough, W. S. (1989). Chemical and isotopic systematics of oceanic basalts: implications for mantle composition and processes. Geological Society, London, Special Publications, 42(1), 313–345. https://doi.org/10.1144/GSL.SP.1989.042.01.19

Syracuse, E. M., van Keken, P. E., & Abers, G. A. (2010). The global range of subduction zone thermal models. Physics of the Earth and Planetary Interiors, 183(1–2), 73–90. https://doi.org/10.1016/j.pepi.2010.02.004

Tatsumi, Y. (1986). Formation of the volcanic front in subduction zones. Geophysical Research Letters, 13(8), 717–720. https://doi.org/10.1029/GL013i008p00717

Vallejo, C., Winkler, W., Spikings, R. A., Luzieux, L., Heller, F., & Bussy, F. (2009). Mode and timing of terrane accretion in the forearc of the Andes in Ecuador. Geological Society of America Memoirs, 204(0), 197–216. https://doi.org/10.1130/2009.1204(09)

Vigouroux, N., Wallace, P. J., & Kent, A. J. R. (2008). Volatiles in high-K magmas from the Western Trans-Mexican Volcanic Belt: evidence for fluid fluxing and extreme enrichment of the mantle wedge by subduction processes. Journal of Petrology, 49(9), 1589–1618. https://doi.org/10.1093/petrology/egn039

Wanless, V. D., & Shaw, A. M. (2012). Lower crustal crystallization and melt evolution at mid-ocean ridges. Nature Geoscience, 5(9), 651–655. https://doi.org/10.1038/ngeo1552

Winkler, W., Villagómez, D., Spikings, R., Abegglen, P., Tobler, St., & Egüez, A. (2005). The Chota basin and its significance for the inception and tectonic setting of the inter-Andean depression in Ecuador. Journal of South American Earth Sciences, 19(1), 5–19. https://doi.org/10.1016/j.jsames.2004.06.006

Witham, F., Blundy, J., Kohn, S. C., Lesne, P., Dixon, J., Churakov, S. V., & Botcharnikov, R. (2012). SolEx: A model for mixed COHSCl-volatile solubilities and exsolved gas compositions in basalt. Computers & Geosciences, 45, 87–97. https://doi.org/10.1016/j.cageo.2011.09.021

Workman, R. K., & Hart, S. R. (2005). Major and trace element composition of the depleted MORB mantle (DMM). Earth and Planetary Science Letters, 231(1), 53–72.

Yepes, H., Audin, L., Alvarado, A., Beauval, C., Aguilar, J., Font, Y., & Cotton, F. (2016). A new view for the geodynamics of Ecuador: implication in seismogenic sources definition and seismic hazard assessment. Tectonics. https://doi.org/10.1002/2015TC003941

Figures captions and tables

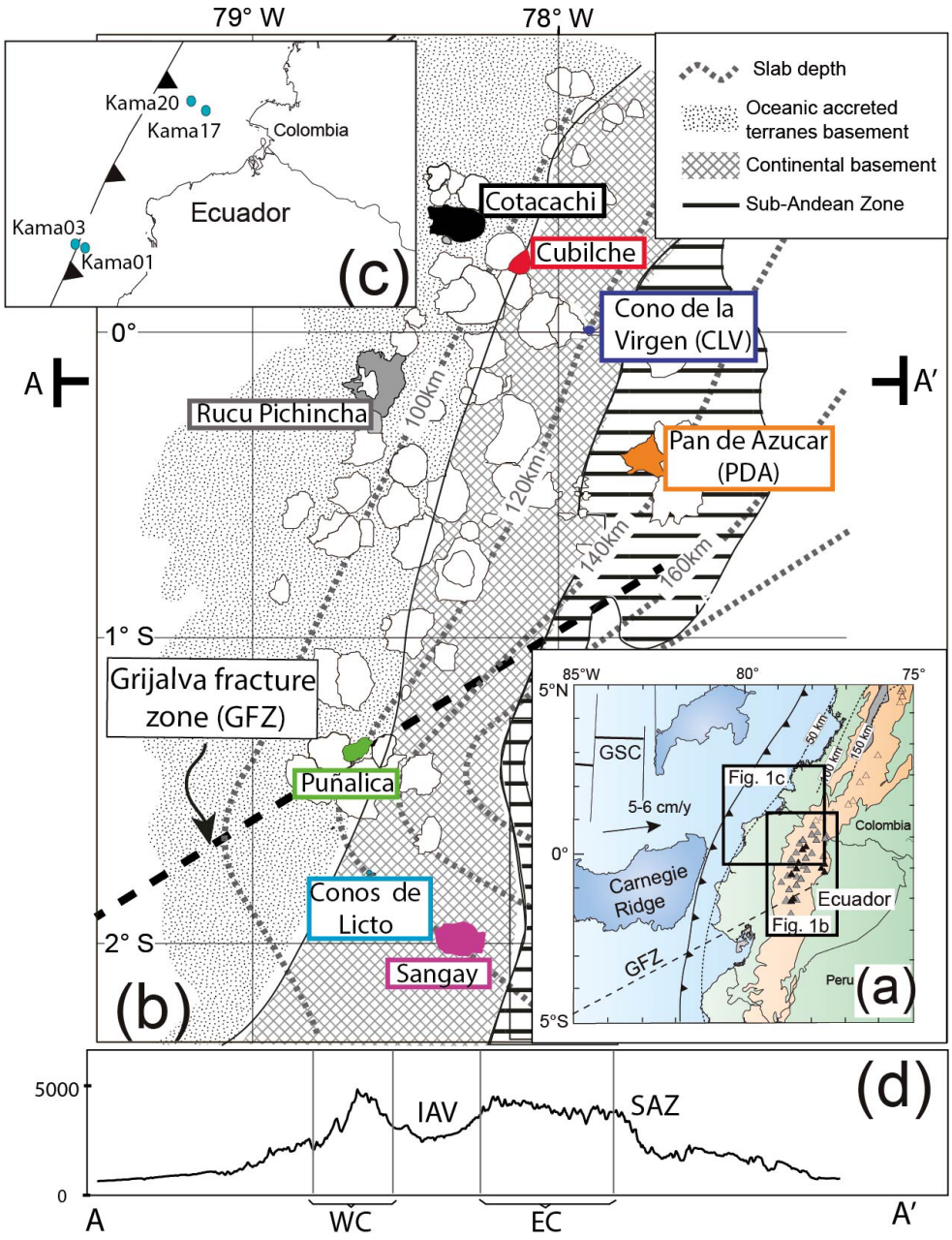

Figure 1 (a) Geodynamic setting of Ecuadorian arc. Shown in black triangles are volcanoes located along the Inter-Andean valley and Sub-Andean zone, and in grey triangles are volcanoes located on the Western and Eastern cordillera. GSC and GFZ stands for Galapagos spreading center and Grijalva fracture zone, respectively. 5-6 cm/y is the convergence rate between the Nazca and South American plate. **(b)** Schematic map of the main geological units in Ecuador [modified from Ancellin et al. (2017) showing Quaternary volcano locations. Analyses of MI were performed in rock samples from Cotacachi, Cubilche, Cono de la Virgen (CLV), Conos de Licto and Sangay. Also shown are Rucu Pichincha, Pan de Azúcar (PDA), and Puñalica volcanoes, whose MI were studied by Le Voyer et al. (2008), and Narváez et al. (2018). The dashed black line is the surface inland projection of the Grijalva fracture zone (GFZ). Slab depth contours are from Yepes et al. (2016). **(c)** Map of Northern Ecuador showing the location of sediments analyzed for this study. Kama 01, 03, 17, and 20 are the names of sedimentary piston cores studied by Ratsov et al. (2010). **(d)** Topographic profile across A-A' in Fig. 1b. WC: Western Cordillera. IAV: Inter-Andean valley. EC: Eastern Cordillera. SAZ: Sub-Andean zone. The color codes for volcanoes shown in this figure are used in subsequent figures to show the provenance of MI.

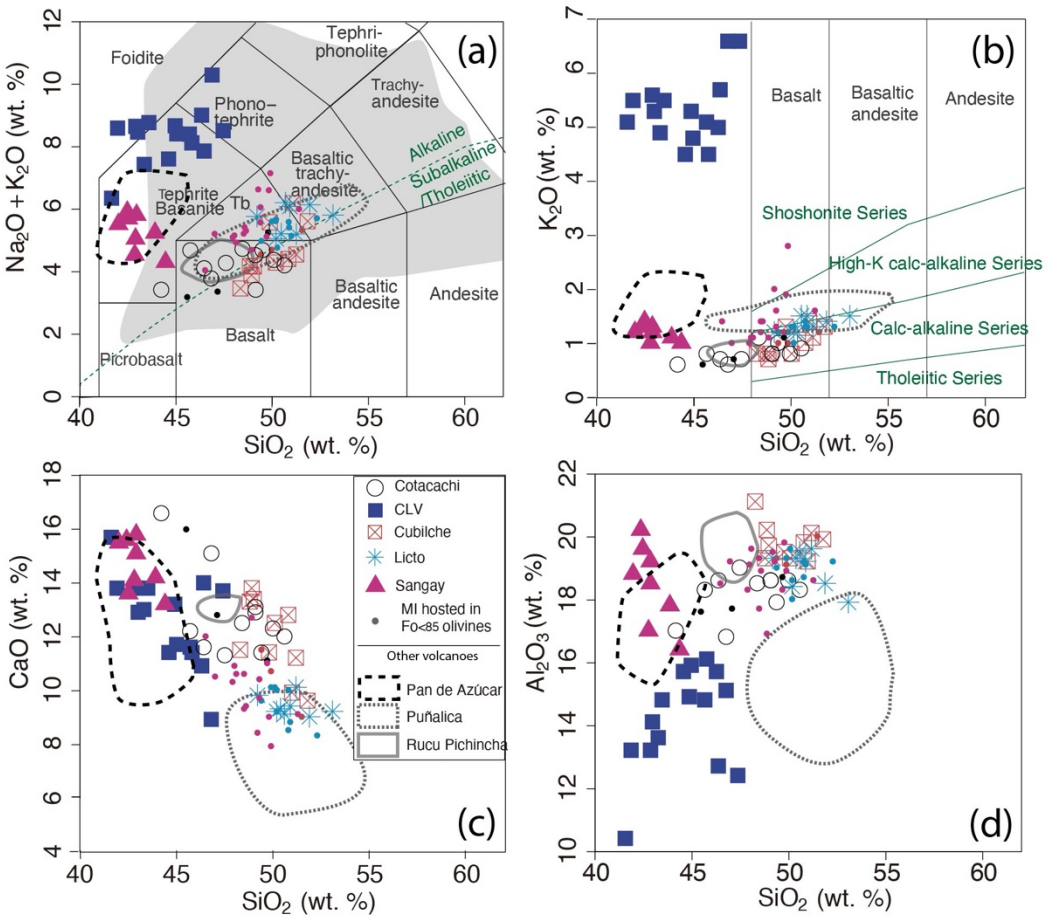

Figure 2 (**a**) SiO_2 *vs.* $Na_2O + K_2O$ classification diagram (Le Bas et al., 1986) of olivine-hosted MI compositions from the Ecuadorian arc. MI are divided in two groups. MI hosted in Fo>85 olivines are shown with larger colored symbols, while those hosted in Fo<85 olivines are depicted with small colored filled circles to show potential compositional variations related to magma evolution. The colors are the same as the volcano color codes in Fig. 1. Sangay MI shown with pink triangles and Puñalica MI compositions from Narváez et al. (2018), PDA, and Rucu Pichincha MI from Le Voyer et al. (2008). The area labeled "Tb" corresponds to trachy-basalt field. The gray shade without a black border is the entire compositional variation of Ecuadorian Quaternary volcanoes rocks (database from Ancellin et al., 2017). (**b**) SiO_2 *vs*. K_2O classification diagram from Peccerillo and Taylor (1976). (**c-d**) Harker diagram of silica versus CaO and Al_2O_3 wt.%. Plotted MI data are uncorrected for post-entrapment modifications, and are normalized for an anhydrous basis.

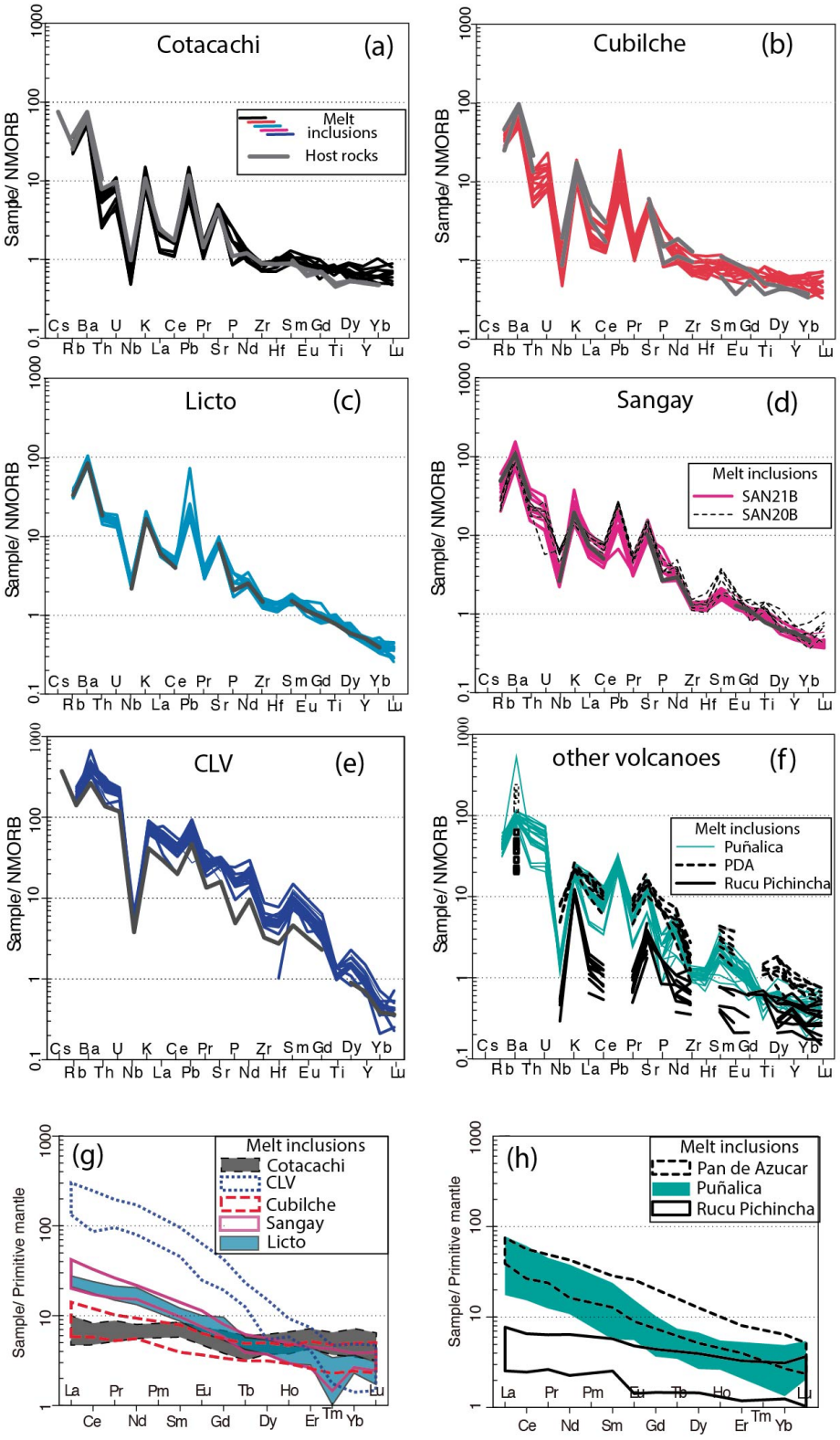

Figure 3 (a-e) Spidergram plot of MI (black and colored lines) and hosted-lava (gray and thick solid lines) compositions from Cotacachi, Cubilche, Licto, Sangay and CLV volcanoes, normalized to N-MORB (Sun & McDonough, 1989). MI labelled SAN20B in (d) from Narváez et al. (2018). **(f)** Spidergram plot similar to (a-e) of MI from Puñalica, PDA, and Rucu Pichincha studied by Le Voyer et al. (2008) and Narváez et al. (2018). **(g)** REE diagram – showing subset of elements used in panels (a)-(f) – for MI compositions of this study normalized to primitive mantle (Sun & McDonough, 1989). **(h)** REE diagram similar to (g) for MI from Puñalica, PDA, and Rucu Pichincha.

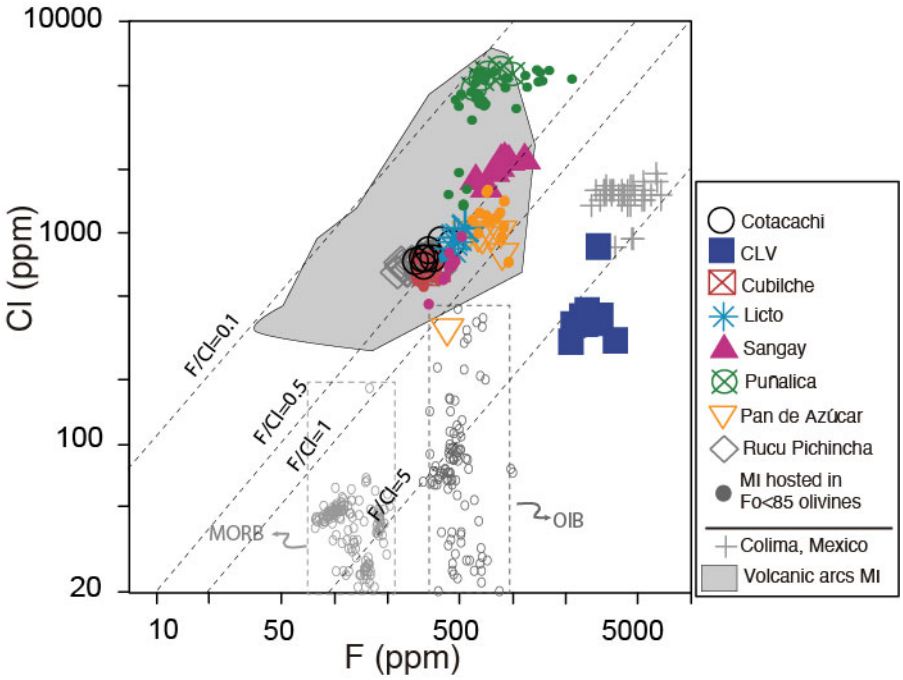

Figure 4 F *vs.* Cl for Ecuadorian MI in logarithmic scale. Sangay MI shown with pink triangles and Puñalica MI compositions from Narváez et al. (2018), PDA, and Rucu Pichincha MI from Le Voyer et al. (2008) and Le Voyer (2009). The volcanic arc MI field is taken from Rose-Koga et al. (2014). Melt inclusion compositions from Colima, Mexico are from Vigouroux et al. (2008). MORB olivine-hosted MI samples from Gakkel Ridge (Shaw et al., 2010), Juan de Fuca Ridge (Wanless & Shaw, 2012) and East Pacific Rise (Wanless & Shaw, 2012). OIB olivine-hosted MI are from Hawaiian volcanoes (Hauri et al, 2002). The colors are the same as the volcano color codes in Fig. 1.

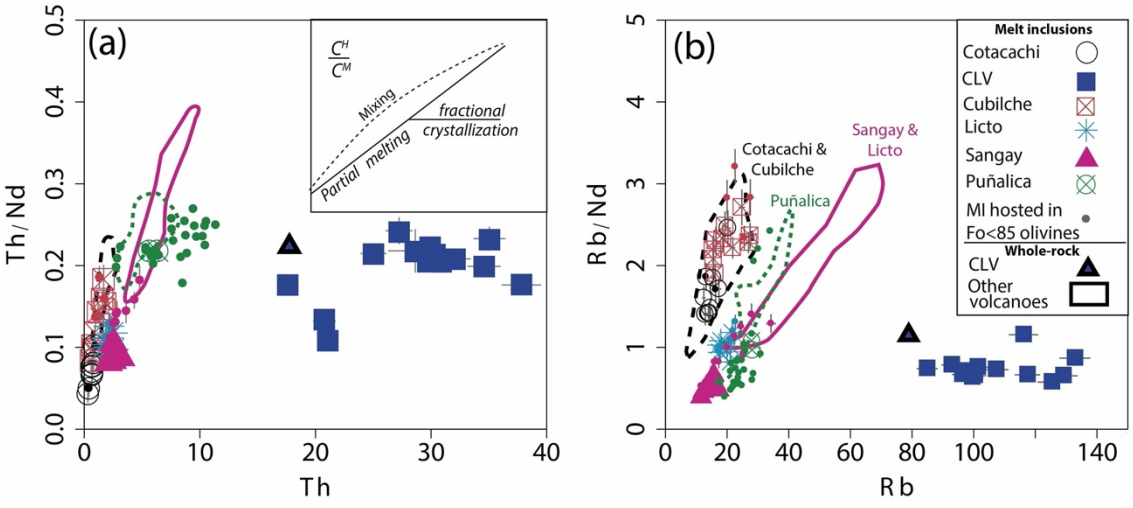

Figure 5 (a-b) C_H *vs.* C_H/C_M diagram where C_H (e.g., Th and Rb) is a highly incompatible element and C_M a moderately incompatible (e.g., Nd) element following the method of Allègre and Minster (1978) to discriminate partial melting or magma mixing from fractional crystallization. Sangay and Puñalica MI compositions from Narváez et al. (2018). Th compositions are not available for PDA and Rucu Pichincha MI. We also show the whole-rock fields for the studied volcanoes.

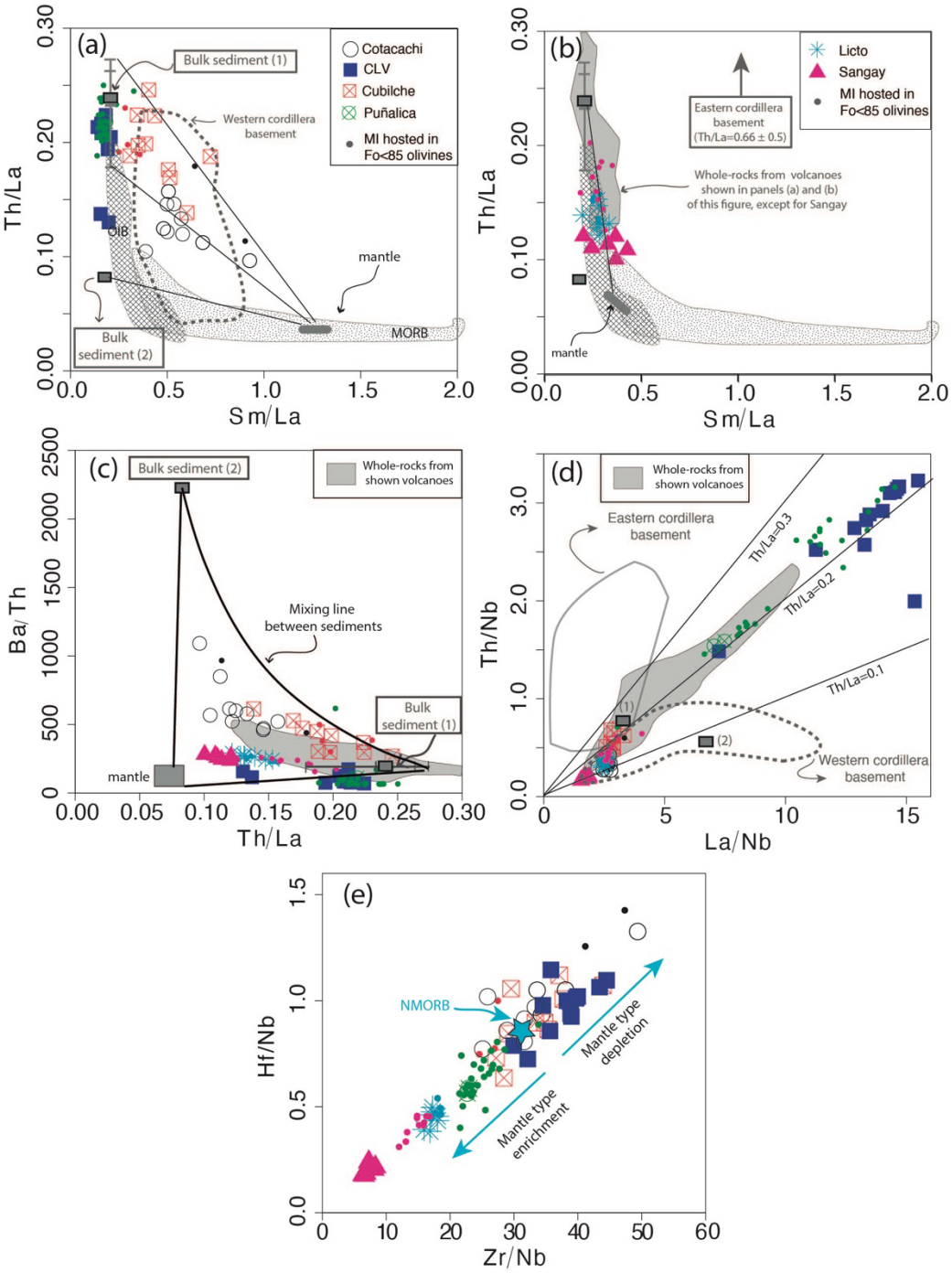

Figure 6 (a-b) Sm/La *vs.* Th/La for MI from **(a)** Puñalica and volcanoes located in the northern part of Ecuador (Cotacachi, Cubilche and CLV), and **(b)** for MI from Licto and Sangay. MORB and OIB fields are from Plank et al. (2005). Hf and Th concentrations are not available for PDA and Rucu Pichincha MI. The Western Cordillera basement field is from Kerr et al. (2002). Eastern Cordillera basement field is from Litherland et al. (1994). Bulk sediment (1) corresponds to newly analyzed terrigenous sediments and (2) to pelagic sediment composition reported by Plank (2014). Sm concentrations are not available for Sangay whole-rocks. **(c)** Th/La *vs.* Ba/Th showing Ecuadorian MI and whole-rocks field for studied volcanoes. Mantle field corresponds to basalts from Carnegie ridge reported by Harpp et al. (2005). For the sake of simplicity, we depicted the whole-rock field for the studied volcanoes as a single grey field. **(d)** La/Nb *vs.* Th/Nb for Ecuadorian MI, whole-rocks from studied volcanoes, and Western and Eastern Cordillera basements. **(d)** Zr/Nb *vs*. Hf/Nb diagram (after Sorbadère et al., 2013) used to discriminate between enriched or depleted mantle-derived melt compositions. Sangay and Puñalica MI compositions from Narváez et al. (2018). Th compositions are not available for PDA and Rucu Pichincha MI.

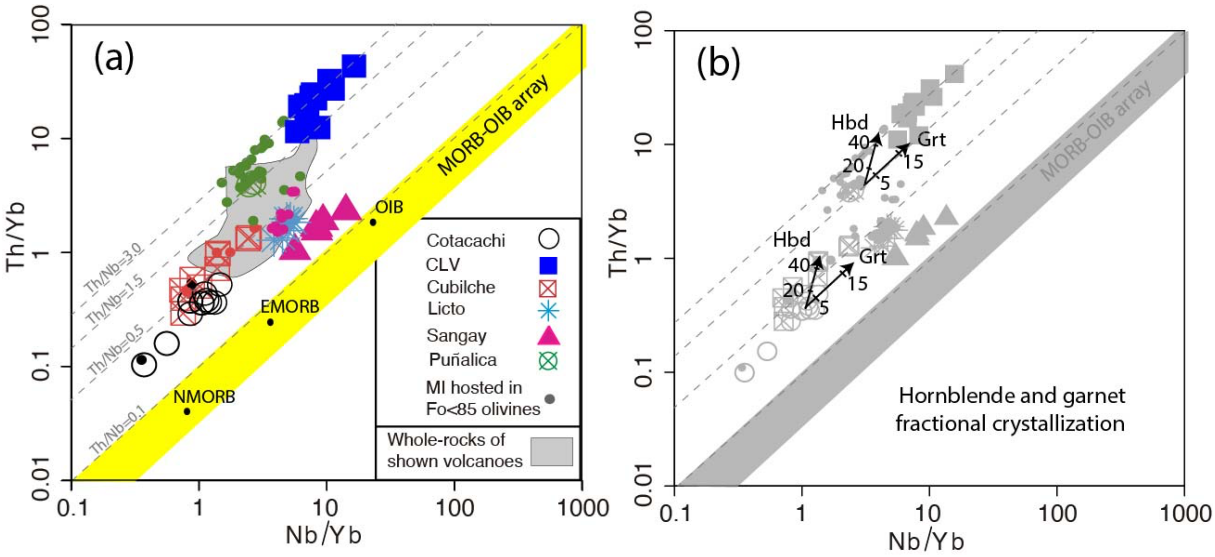

Figure 7 (a-b) Nb/Yb *vs.* Th/Yb of Ecuadorian MI compared to MORB-OIB compositions used to discriminate between conservative and non-conservative elements (Pearce and Peate, 1995). Th compositions are not available for PDA and Rucu Pichincha MI. The grey field in (a) is the entire compositional variation of Ecuadorian Quaternary volcanic rocks (data from Ancellin et al., 2017). The numbers on the black arrows in (b) indicate the degree of fractional crystallization of a mono-mineral cumulate composed of hornblende or garnet, respectively, using $D^{mineral/melt}$ for individual minerals in contact with basaltic melts given by Green et al. (2000). The corresponding arrows for other typical minerals (plagioclase, pyroxenes) are smaller than the size of the symbols. Sangay and Puñalica MI compositions from Narváez et al. (2018).

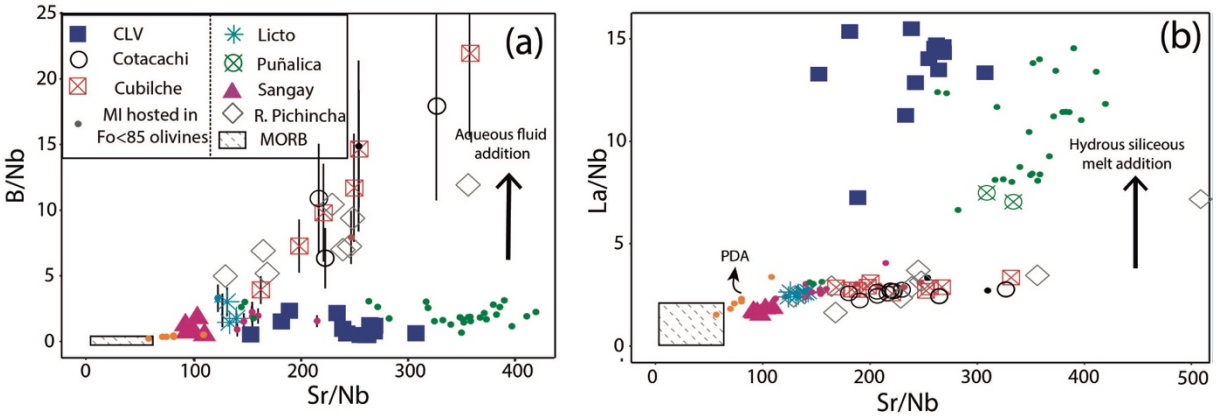

Figure 8 (a) Sr/Nb *vs*. B/Nb and **(b)** Sr/Nb *vs*. La/Nb for Ecuadorian MI. Propagated standard error bars (±1σ) of new data are shown in vertical lines in (a). The hatched boxes in (a) and (b) are MORB fields based on data from Leroux et al. (2006) and Chaussidon and Marty (1995). Sangay and Puñalica MI compositions from Narváez et al. (2018), PDA, and Rucu Pichincha MI from Le Voyer et al. (2008)

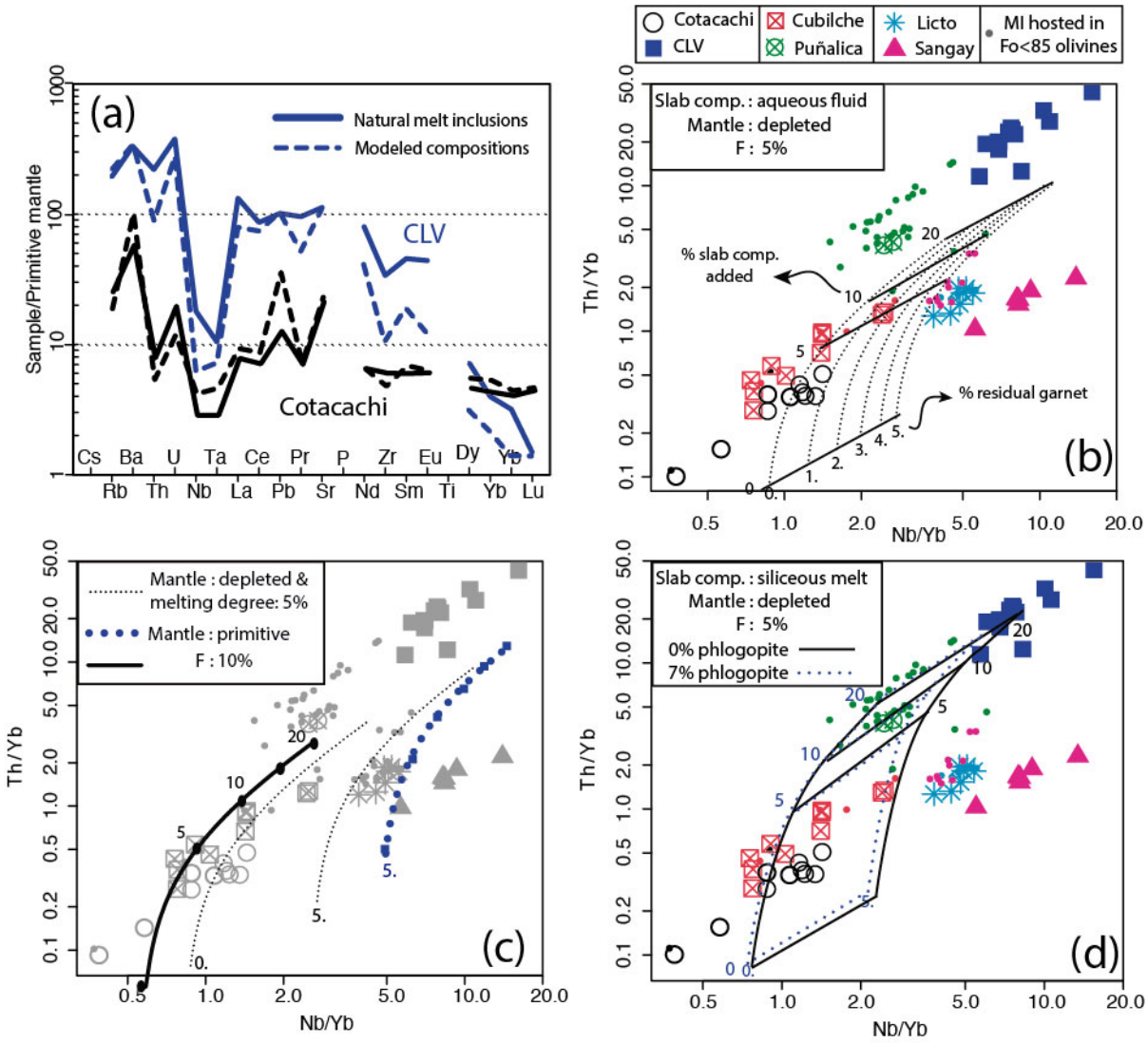

Figure 9 (a) Selected trace element composition of natural MI (colored solid lines), compared to modelled compositions (colored dashed lines) for two contrasting MI compositions (Cotacachi and CLV). MI compositions were reproduced using a modified version of ABS to apply the batch melting model. The degree of mantle melting is set to 5%. The slab component for CLV is a hydrous siliceous melt, while, for Cotacachi, it is an aqueous fluid. Detailed parameters are given in Table 5 and in the text. **(b-d)** Nb/Yb *vs.* Th/Yb, similar to Fig. 7a, but showing the results of geochemical modelling. **(b)** Results of an aqueous fluid-like component added to a depleted mantle (Workman & Hart, 2005). The grid formed by dotted and solid lines are results obtained at different garnet % left in the residue from mantle melting (dotted lines representing contours), and slab component percentage (solid lines, up to 20%) added to the mantle wedge. The degree of mantle melting is 5%, and the residual mineralogy is ol-opx-cpx in a proportion of 58:26:16. **(c)** Influence of mantle composition and degree of melting compared to the field shown in (b). Solid line is the results for 10% of mantle melting while keeping all parameters constant (residual garnet is 0%), and dotted blue line shows the result for primitive mantle composition (residual garnet is 5%). Model with primitive mantle reproduces MI composition with higher Nb/Yb. The grey symbols are those in (b). SAN20B MI (pink triangles outside the modeled grid) are reproducible when we consider them to contain amphibole-bearing clinopyroxenite derived melts (*cf.* Narváez et al., 2018). **(d)** Results obtained under the same condition as (b), but with a hydrous siliceous melt-like component added to the mantle wedge. The solid line grid represents the results calculated with a residual source without phlogopite, and the dotted line grid with 7% phlogopite. CLV MI that plot off the grid can be reproduced with a lower degree of mantle melting or higher garnet % left in the residue. Phlogopite partition coefficients are from Halliday et al. (1995), and that for thorium from LaTourrette et al. (1995).

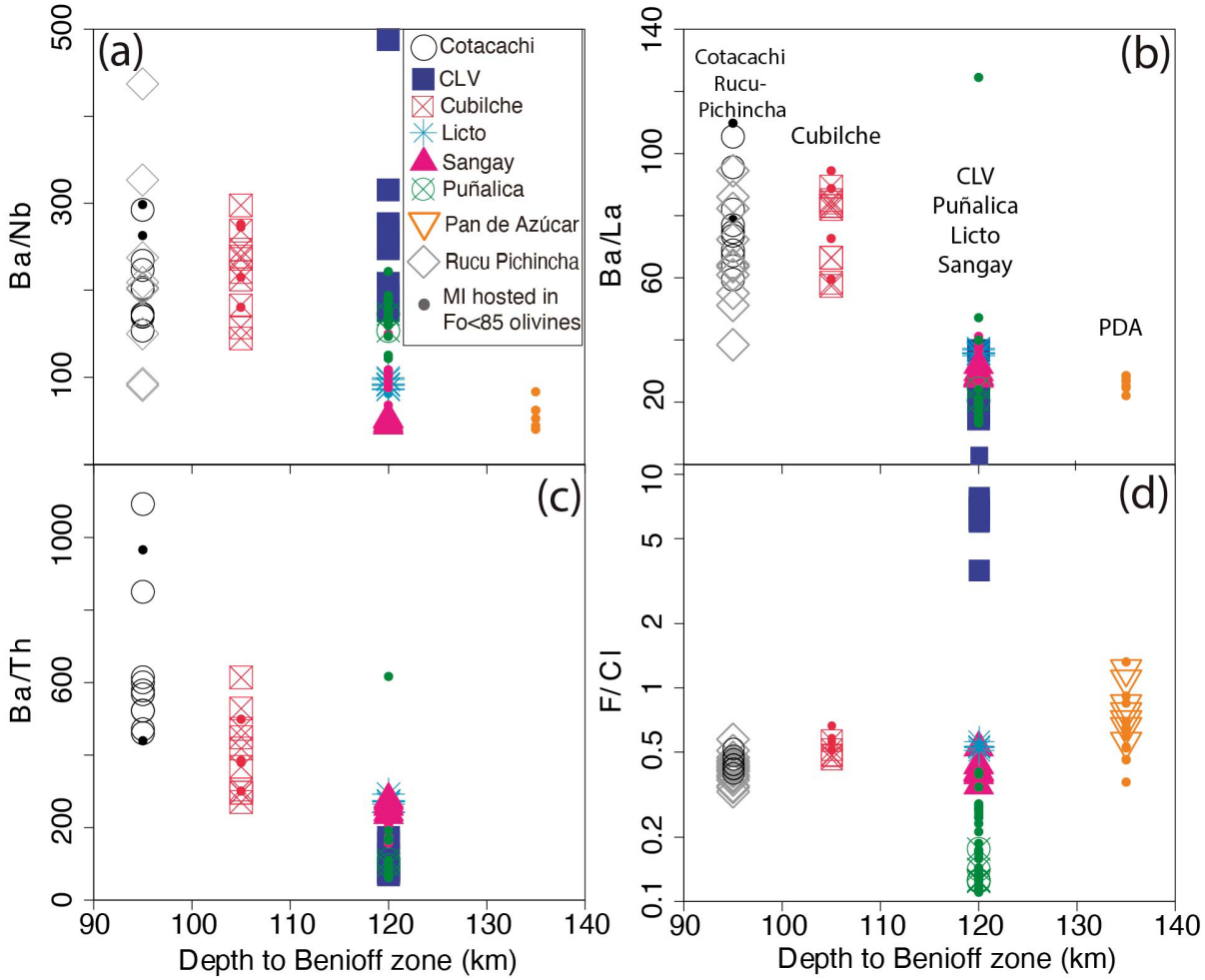

Figure 10 (a-c) Ba/Nb, Ba/La, Ba/Th plotted against the depth to the Benioff zone under each volcano. The numerator (Ba) is an element that is abundant in the slab component, and the denominators are substantially less mobile elements. **(d)** F/Cl *vs.* depth to the Benioff zone with in logarithmic scale. Sangay MI shown with pink triangles and Puñalica MI compositions from Narváez et al. (2018), PDA, and Rucu Pichincha MI from Le Voyer et al. (2008) and Le Voyer (2009).

Table 1. Major and trace element concentration of hosting rocks. Units for major and trace elements are wt.% and ppm, respectively.

Volcano	*Cotacachi*			*Cubilche*		*Cono de la Virgen*			*Licto*	*Sangay*
Sample code	17EQ91	MM1B	COTA02	17EQ81	17EQ95	CAY45A	CAY45B	CAY45C	RIO10B	SAN21B
Rock name	Basaltic andesite	Basaltic andesite	Basaltic andesite	Andesite	Andesite	Trachy-andesite	Trachy-andesite	Trachy-andesite	Basaltic andesite	Basaltic trachy-andesite
IGSN	IEDFN0001	IEDFN0002	IEDFN0003	IEDFN0004	IEDFN0005	IEDFN0006	IEDFN0007	IEDFN0008	IEDFN0009	IEDFN000A
Deposit	lava flow	tephra bomb	lava flow	lava flow	lava flow	lava flow	lava flow	lava flow	lava flow	lava flow
Mineral assemblage	pl+cpx+opx+ol			pl+cpx+opx+ol		pl+amph+opx+cpx+ol			pl+opx+ol	pl+opx+ol
SiO_2	56.9	55.2	56.3	58.0	59.5	59.9	60.0	59.6	53.3	54.0
TiO_2	0.6	0.7	0.6	0.7	0.5	0.8	0.8	0.9	1.0	1.0
Al_2O_3	16.1	15.3	15.4	17.3	16.8	15.2	15.2	15.1	16.0	18.1
FeOt	7.4	8.2	7.8	6.6	6.2	5.7	5.6	5.7	8.2	7.5
MnO	0.1	0.2	0.1	0.1	0.1			0.1	0.1	0.1
MgO	6.8	7.9	7.8	4.8	5.3	4.6	4.6	4.8	8.3	5.1
CaO	8.0	8.8	8.2	7.1	7.0	6.6	6.4	6.6	8.1	8.3
Na_2O	3.0	2.9	2.9	3.9	3.5	3.7	3.7	3.6	3.6	4.1
K_2O	1.1	0.8	0.8	1.3	1.0	2.9	2.9	3.0	1.2	1.4
P_2O_5	0.1	0.1	0.1	0.2	0.1	0.6	0.6	0.6	0.2	0.3
Mg#	62.2	63.4	64.0	56.7	60.1	58.9	59.0	60.2	64.3	54.6
Sc	27.5	31.9	28.2	18.7	23.5			15.3	20.2	19.0
V	185.0	209.5	205.5	163.4	152.9			147	200.0	212.0
Rb	20.9	15.9	14.3	26.1	14.2			79.3	18.5	28.0
Sr	371	389	375	557	443			1427	720	920
Y	14.5	15.8	14.2	12.0	12.5			18.9	14.4	16.3
Zr	63.5	66.6	67.1	98.7	73.4			236	110.0	96.0
Nb	2.6	2.3	1.2	4.6	2.1			8.7	5.1	6.1
Ba	475	399	444	615	581			1687	526	700
La	6.5	6.1	7.2	13.2	8.1			72.7	15.0	18.5
Ce	14.0	13.2	15.9	23.4	13.3			149	30.0	38.0
Nd	8.5	8.9	9.4	14.1	8.5			69.5	18.5	21.4
Sm	2.5	2.4	2.6	3.0	1.7			11.9	4.0	
Eu	0.7	0.8	0.6	1.0	0.4			3.2	1.2	1.3
Gd	2.6	2.6	2.6	2.8	2.1			8.3	3.6	4.0
Dy	2.4	2.6	2.5	2.2	2.0			4.0	2.7	2.9
Er	1.1	1.5	1.2	0.8	0.8			1.5	1.3	1.6
Yb	1.5	1.5	1.5	1.1	1.2			1.1	1.2	1.4
Th	1.3	1.0	1.3	2.6	1.6			16.4	2.2	3.7
Reference	*A*	*B*	*A*	*A*	*A*	*C*	*C*	*C*	*B*	*D*

Note. The rock names are based on TAS classification after Le Bas et al. (1986). Mg# is calculated as 100*molar (MgO/(MgO+FeOT)). Olivine represents less than 5 vol.% in all rock samples. A, This study. B, Ancellin et al. (2017). C, Samaniego et al. (2005). D, Monzier et al. (1999).

Table 2. Major and trace element concentration of sediment samples. Units for major and trace elements are wt.% and ppm, respectively.

Sample name	*S-K01-2*	*S-K03-2*	*S-K03-4*	*S-K17-T4*	*S-K20-3*
Core name	Kama01	Kama03	Kama03	Kama17	Kama20
Location	margin slope	trench	trench	Manglares basin	Manglares basin
Latitude	N 0°16.70'	N 0°18.89'	N 0°18.89'	N 1°43.08'	N 1°49.33'
Longitude	W 80°43.4'	W 80°49.65'	W 80°49.65	W 79°27.8'	W 79°7.8'
Water depth (m bsl)	3046.0	3797.0	3797.0	865.0	606.0
SiO_2	64.6	64.6	62.6	57.7	57.7
TiO_2	0.6	0.5	0.6	0.6	0.6
Al_2O_3	15.7	15.3	14.9	17.5	17.4
FeOt	5.2	4.9	5.6	6.3	5.8
MnO	0.0	0.1	0.0	0.0	0.1
MgO	2.7	2.6	3.1	3.1	3.0
CaO	4.4	5.3	6.0	8.5	9.7
Na_2O	4.8	5.0	5.0	4.1	4.2
K_2O	1.8	1.7	1.9	1.8	1.4
P_2O_5	0.2	0.2	0.2	0.2	0.1
Total	85.5	87.3	81.8	79.7	89.2
Rb	34.2	33.0	39.9	34.4	27.7
Sr	279.2	333.9	284.2	337.7	456.2
Ba	734.4	786.3	667.5	591.8	561.1
Sc	13.2	12.2	14.3	16.1	16.3
V	104.1	103.4	114.9	123.0	136.7
Cr	72.6	64.1	81.5	86.0	81.1
Co	9.2	9.0	8.9	11.2	14.4
Ni	35.7	30.0	42.6	46.2	31.5
Y	11.1	10.1	13.6	12.7	10.3
Zr	66.2	70.2	58.2	61.7	68.4
Nb	3.2	2.7	2.2	4.5	2.8
La	9.4	8.8	9.6	12.0	9.7
Ce	18.9	18.2	17.3	24.4	19.8
Nd	9.4	9.0	10.1	10.5	11.0
Sm	2.0	2.0	2.2	2.0	2.4
Eu	0.6	0.6	0.6	0.6	0.8
Gd	2.4	2.1	2.1	2.3	2.4
Dy	1.7	1.6	1.8	1.8	2.1
Er	1.4	1.2	1.1	0.9	1.4
Yb	0.9	0.9	1.1	1.0	1.1
Th	2.2	1.6	2.6	3.2	2.3
Th/La	0.23	0.18	0.27	0.26	0.23
Sm/La	0.21	0.23	0.23	0.17	0.25

0

Table 3 Major, trace and volatile element concentrations of olivine-hosted melt inclusions from Cayambe, Cotacachi, Cubilche, Conos de Licto and Sangay volcanoes, normalized to an anhydrous basis.

	Cayambe *CAY45C*										*CAY45A*			*CAY45B*				***Cotacachi*** *17EQ91*		
	3A_1	3A_2	3A_3	5A_1	5A_2	1A	3C	4B	5C	6A	2B	3A	3B	1A	4A	5A	6A	1A_c	1A_r	1C
SiO_2	43.0	42.9	43.3	46.3	45.0	46.4	45.7	45.8	41.9		44.9		43.5	47.4	41.6	46.8	44.6	44.2	45.5	49.1
TiO_2	1.3	1.6	1.4	1.2	1.5	1.7	1.3	1.4	1.7		1.7		1.8	1.4	1.7	1.7	1.4	1.0	1.0	1.0
Al_2O_3	14.1	13.2	13.6	15.7	15.9	12.7	14.8	16.1	13.2		14.9		14.8	12.4	10.4	15.1	15.7	17.0	17.6	18.6
FeOt	9.8	9.5	9.8	7.1	7.7	5.9	6.8	6.8	10.2		7.0		6.4	6.0	12.5	8.1	7.8	8.4	7.9	5.4
MnO	0.1	0.1	0.0	0.1	0.1	0.1	0.1	0.1	0.2		0.1		0.1	0.1	0.1	0.1	0.1	0.1	0.1	0.1
MgO	8.9	8.5	9.3	8.1	7.8	9.6	9.6	8.7	8.4		7.8		9.2	8.2	8.9	8.0	9.4	9.2	8.6	9.3
CaO	12.9	13.8	13.0	10.9	11.7	14.0	11.6	11.4	13.8		13.2		13.8	13.7	15.7	8.9	11.4	16.6	16.0	12.9
Na_2O	3.1	3.1	2.5	4.0	3.6	2.2	3.3	3.6	3.1		3.4		3.3	2.0	1.2	3.7	3.1	2.8	2.6	2.6
K_2O	5.3	5.6	4.9	5.0	4.8	5.7	5.1	4.5	5.5		5.3		5.5	6.6	5.1	6.6	4.5	0.6	0.6	0.8
P_2O_5	1.4	1.9	2.0	1.6	1.8	1.8	1.9	1.6	2.0		1.7		1.6	2.3	2.8	1.1	2.0	0.0	0.2	0.2
Total	96.7	96.5	97.0	98.4	95.6	97.4	97.8	97.4	96.1		98.1		96.3	95.4	97.0	98.1	93.6	98.8	102.1	101.3
F	2030		1968	1749		2214	1945		2388	2969	2078		2079	2471		1703				326
Cl	396		397	385		395	430		1018	310	465		418	432		305				957
S	5265		5245	4239		2968	5224		6516		5448		5448	5924		3640				749
B			7.7	<12.8		10.7	11.9	<49	<10.7	16.4	<11.1	<14.6	13.2	<11.3	<16.7	28.1	<11.7	20.1	<19.4	12.1
Sc			29.3	14.7		33.6	24.9	28.0	30.9	29.9	23.0	<3.33	22.9	18.9	30.6	13.0	19.9	73.0	67.2	50.6
V			285	308		289	267	307	301	311	274	57	289	226	324	201	258	488	461	293
Rb			96	85		117	97	101	100	129	100		107	133	125	116	93	13.0	13.0	15.3
Sr			2586	2406		2558	2589	2649	2682	1914	2696	1451	2721	2899	2244	2239	2719	367	351	422
Y			26.1	21.9		31.7	25.4	25.2	26.9	34.6	28.0	25.6	26.6	27.0	41.0	17.1	22.6	23.4	23.2	18.6
Zr			374	319		477	375	407	410	365	423		402	395	638	355	339	55.5	53.8	63.7
Nb			9.7	9.9		10.7	9.7	11.4	10.3	10.6	10.6		10.3	11.1	14.7	11.9	8.9	1.1	1.1	1.9
Ba			2450	2066		2875	2475	2005	2612	3329	2645	2397	2554	3060	2848	2189	4324	329	339	381
La			141	128		166	138	128	150	162	148	152	139	163	195	86	118	3.1	3.1	5.1
Ce			282	248		348	279	249	306	363	300	313	294	331	411	145	243	8.5	8.2	12.0
Pr			34.3	30.5		40.8	32.1	33.1	35.2	44.6	36.2	38.1	35.2	38.7	49.9	24.3	28.1	1.4	1.3	1.8
Nd			142	113		174	135	132	154	195	151	155	145	151	214	100	117	7.0	6.9	8.2
Sm			24.3	18.8		30.5	23.0	24.2	25.5	33.2	24.8	24.7	25.3	26.9	39.0	18.5	21.0	2.9	2.8	2.5
Eu			6.3	5.2		7.9	6.0	3.8	6.5	8.5	6.6	5.6	6.4	6.9	9.8	6.8	5.2	0.9	1.1	0.9
Gd			15.2	10.5		18.1	13.5	14.5	16.5	21.0	16.3	15.1	14.4	15.6	23.2	10.8	12.1	2.7	3.1	2.9
Tb			1.5	1.3		1.7	1.4	2.0	1.6	2.1	1.5	1.6	1.5	1.5	2.3	1.3	1.2	0.5	0.6	0.5
Dy			6.8	6.3		8.2	6.4	3.7	7.0	8.9	6.9	6.7	6.8	6.8	10.2	4.9	6.3	3.9	4.2	3.1
Ho			0.9	0.9		1.2	1.0	1.0	1.1	1.2	1.1	0.9	0.9	1.0	1.4	0.9	0.9	1.0	0.9	0.7
Er			2.0	2.0		2.7	2.0	3.2	2.1	2.6	2.2	1.8	2.2	2.3	2.7	2.0	1.8	2.7	3.1	2.3
Tm			0.2	0.1		0.3	0.2	<0.16	0.3	0.3	0.2	0.2	0.3	0.2	0.3	0.1	0.2	0.4	0.4	0.3
Yb			1.6	0.6		1.4	1.2	1.0	1.4	1.8	1.5	1.2	1.5	1.1	2.1	1.4	1.1	3.0	3.2	1.8
Lu			0.2	0.1		0.2	0.2	0.3	0.2	0.2	0.2	0.2	0.2	0.2	0.2	0.1	0.2	0.4	0.4	0.3
Th			30.3	27.2		34.6	29.9	28.6	32.1	21.1	30.9	20.8	29.7	35.1	37.8	17.6	25.0	0.3	0.4	0.6
Pb			25.2	15.9		26.1	20.3	17.4	27.2	8.2	22.6		24.0	28.3	13.5	15.2	18.1	2.0	1.8	1.9
U			9.2	9.0		10.4	9.7	9.0	9.7	5.3	9.7	5.1	9.8	11.0	8.3	7.6	8.6	0.2	0.3	0.4
Hf			9.6	7.2		11.8	9.1	13.0	10.4	10.3	10.8	2.0	9.5	9.5	15.6	9.4	8.9	1.5	1.6	2.0
Ta			0.4	0.2		0.4	0.4	0.6	0.4	3.0	0.5	1.2	0.3	0.4	0.6	0.4	0.3	<0.12	<0.11	0.1
Fo	89.1	89.3	89.1	87.1	87.1	89.9	88.4	86.3	89.4	89.8	87.5		89.5	89.6	89.3	86.3	86.9	85.4	84.7	87.9

Note. The total given are the measured values. *Fo*=100*molar (Mg/Mg+Fe) of hosting olivines. "<" concentrations under the detection limit.

Table 3 continued

	Cotacachi *17EQ91*					*COTA02*			*MM-1B*			***Cubilche*** *17EQ81*								
	2B	2C	4C	5C	7A_b	2A_b	2A_m	2A_t	1B	5B	6A	1B	1C	1E	2A_b	2A_t	2B_c	2C	3C_b	3C_t
SiO_2	46.8	47.1	49.7	49.4	48.4	50.6	50.0	49.1	47.5	45.7	46.4	50.8	51.0	48.9	49.0	48.8		50.1	51.8	51.2
TiO_2	0.8	0.9	0.9	0.7	0.9	1.0	0.9	1.1	1.0	1.0	0.9	0.8	0.9	0.7	0.8	0.8		0.6	1.1	0.8
Al_2O_3	16.8	17.7	18.7	17.9	18.5	18.3	18.6	18.6	19.0	18.3	18.6	19.8	19.2	20.2	19.7	19.3		19.3	19.9	20.1
FeOt	6.6	9.2	5.8	6.4	5.5	5.3	5.4	4.8	7.6	7.4	8.0	4.5	4.9	5.3	4.9	5.2		5.6	4.8	5.0
MnO	0.1	0.1	0.1	0.1	0.1	0.1	0.1	0.1	0.1	0.1	0.1	0.1	0.1	0.0	0.0	0.1		0.1	0.1	0.0
MgO	9.8	8.6	8.3	9.3	9.2	8.2	8.0	8.4	9.1	10.6	10.2	6.9	7.5	7.1	7.8	8.0		7.2	6.8	6.9
CaO	15.1	12.8	11.1	11.4	12.5	12.0	12.3	13.1	11.3	12.2	11.6	12.8	9.9	13.8	13.4	13.3		12.5	9.6	11.2
Na_2O	3.2	2.6	4.1	3.7	3.7	3.3	3.6	3.7	3.6	3.9	3.4	3.4	4.8	3.2	3.3	3.4		3.5	4.3	3.5
K_2O	0.6	0.7	1.1	1.0	1.1	0.9	0.8	0.8	0.7	0.8	0.7	1.0	1.4	0.7	0.8	0.8		0.8	1.3	1.1
P_2O_5	0.3	0.2	0.1	0.1	0.1	0.2	0.2	0.3	0.2	0.1	0.1	0.0	0.3	0.1	0.1	0.2		0.2	0.2	0.2
Total	101.3	99.6	100.1	97.7	98.6	100.3	100.1	100.1	100.5	98.5	99.3	101.4	97.7	100.7	100.8	100.1		100.6	99.0	100.7
F	283				369	417		341	308	300	312	320		320	325		419	315	360	
Cl	843				1082	1040		871	799	878	876	776		739	815		779	801	770	
S	1226				832	686		577	1339	1375	1295	1772		871	851			867	525	
B	<16.8	23.8			<19.7	<20	<17.8	23.2	<15.2	<16.5	<8.6	22.5	13.0	24.9	<16.3	18.1	<8.9	17.4	<16	<8.6
Sc	74.4	52.6			38.2	18.1	19.1	23.7	24.7	22.8	32.4	34.1	15.7	31.8	31.4	26.3	12.5	18.4	15.6	25.6
V	464	334			299	409	298	392	344	356	330	329	227	357	377	381	204	344	243	265
Rb	12.3	16.1			20.1	12.8	13.8	14.1	17.2	14.4	13.7	18.4	26.8	15.2	15.5	16.2	25.4	19.2	27.3	21.7
Sr	365	406			427	442	449	461	451	448	435	391	534	407	383	386	542	393	528	445
Y	21.1	19.4			17.4	15.6	16.5	16.0	15.5	18.7	17.8	17.6	13.8	17.4	17.1	17.7	12.1	17.8	13.9	15.8
Zr	52.6	65.9			66.9	55.4	68.6	67.3	62.8	65.0	66.0	58.1	89.5	50.0	52.7	54.9	71.0	52.6	89.0	74.0
Nb	1.4	1.6			2.0	2.1	2.2	2.1	2.5	2.0	2.3	1.5	3.3	1.1	1.4	1.6	2.9	1.8	3.1	2.2
Ba	323	421			435	363	369	368	384	396	392	397	534	318	342	360	522	380	516	460
La	3.4	5.3			5.3	5.7	5.4	5.5	6.5	5.4	5.1	4.4	9.1	3.8	4.1	4.2	8.8	4.6	9.0	6.9
Ce	9.5	12.5			12.4	13.5	13.8	12.8	12.5	12.6	12.5	10.9	20.1	9.6	10.8	10.5	19.0	10.1	20.0	15.3
Pr	1.5	1.8			1.7	2.0	2.0	1.8	2.2	1.9	1.8	1.5	2.6	1.3	1.5	1.4	2.3	1.5	2.2	2.1
Nd	7.6	9.4			8.2	9.1	9.7	9.9	10.0	9.7	9.6	7.9	11.7	6.9	7.4	7.0	10.8	7.7	11.5	9.7
Sm	2.3	3.4			2.7	2.9	2.9	2.7	2.5	3.1	2.9	2.3	3.2	2.7	2.1	2.6	2.6	1.8	2.8	2.4
Eu	0.8	1.1			0.9	1.0	0.7	0.8	0.9	0.8	0.9	0.6	0.9	0.8	0.8	0.8	0.8	0.7	1.0	0.9
Gd	3.2	3.7			2.6	2.1	3.7	2.8	3.0	3.1	2.9	2.4	3.0	2.9	2.2	2.3	2.6	2.8	2.1	2.6
Tb	0.5	0.6			0.4	0.5	0.5	0.3	0.5	0.5	0.5	0.4	0.5	0.4	0.4	0.4	0.4	0.4	0.4	0.4
Dy	3.9	4.0			3.1	2.8	3.4	2.5	2.9	3.1	3.1	3.0	2.6	3.1	3.4	2.9	2.4	2.7	2.4	3.0
Ho	0.8	0.7			0.6	0.6	0.7	0.6	0.7	0.8	0.6	0.5	0.5	0.7	0.6	0.7	0.5	0.5	0.5	0.6
Er	2.3	2.2			2.2	1.9	2.3	1.9	1.9	2.1	2.0	2.0	1.6	1.8	2.3	2.2	1.3	2.2	1.3	1.6
Tm	0.4	0.4			0.3	0.3	0.4	0.3	0.3	0.3	0.3	0.3	0.2	0.3	0.3	0.3	0.2	0.3	0.2	0.2
Yb	2.5	1.8			2.3	1.8	1.5	1.9	1.9	2.3	1.9	1.5	1.3	1.5	1.9	2.1	1.1	1.3	1.3	1.6
Lu	0.4	0.3			0.3	0.3	0.2	0.2	0.2	0.3	0.3	0.3	0.2	0.3	0.3	0.2	0.2	0.3	0.2	0.2
Th	0.4	1.0			0.8	0.7	0.8	0.8	0.7	0.6	0.7	0.8	1.8	0.7	0.7	0.6	1.7	0.9	1.7	1.6
Pb	1.8	3.0			3.5	2.3	2.1	2.1	4.5	3.0	2.9	2.7	3.8	2.0	2.2	2.2	4.5	3.0	5.3	7.7
U	0.2	0.4			0.5	0.5	0.5	0.5	0.4	0.4	0.4	0.5	0.8	0.4	0.5	0.4	0.7	0.6	0.7	0.7
Hf	1.5	2.0			1.8	2.2	2.0	1.7	1.9	1.9	2.0	1.6	2.4	1.2	1.6	1.3	2.2	1.9	2.0	2.0
Ta	<0.1	0.1			0.1	<0.12	0.2	0.1	0.1	<0.1	0.2	<0.12	0.2	<0.11	<0.12	<0.11	0.1	<0.13	0.3	0.1
Fo	87.2	84.3	84.8	85.6	85.9	86.2	86.2	86.7	85.2	87.1	85.7	88	86.3	87.2	88.3	87.1	80.4	85.5	85.9	85.9

Table 3 continued

	Cubilche *17EQ81*			*17EQ95*			***Conos de Licto*** *RIO10B*												
	3D	5A	5B	1B	2A	4B	1A	1B	1B_l	1B_t	1C	1D	2A	2B	2D	3A_l	3A_lc	3A_rc	3B_b	3B_c
SiO_2	49.9	49.8	51.5		49.4	48.3	51.2	50.9	50.2	50.2	49.2	50.6	50.2	50.8	49.4	50.8	49.9	50.1	53.1	51.9
TiO_2	0.9	1.1	0.7		0.8	0.7	1.1	1.1	1.1	1.0	1.2	1.3	1.0	1.3	1.2	1.4	1.4	1.3	1.1	1.0
Al_2O_3	19.1	19.5	20.0		19.3	21.1	19.6	19.1	18.6	18.0	19.3	19.5	18.4	18.7	19.0	19.2	19.3	19.6	17.9	18.5
FeOt	6.1	5.5	5.7		6.3	6.6	6.3	7.2	7.3	8.5	6.6	6.3	7.1	6.8	7.4	6.7	7.0	6.9	6.2	6.7
MnO	0.1	0.1	0.1		0.1	0.1	0.0	0.1	0.1	0.2	0.1	0.1	0.1	0.1	0.1	0.1	0.2	0.1	0.1	0.0
MgO	8.4	6.7	7.6		8.0	8.0	6.1	7.2	7.7	7.2	7.7	6.5	8.7	7.8	8.1	6.1	6.1	6.0	6.3	6.4
CaO	10.7	11.4	9.0		11.5	11.5	10.1	8.8	9.2	10.0	9.8	9.1	9.2	8.5	9.6	10.0	10.1	10.1	9.2	9.0
Na_2O	3.7	4.2	4.1		3.6	2.6	3.9	3.9	4.4	3.8	4.5	4.7	3.9	4.2	3.8	4.1	4.4	4.3	4.3	4.7
K_2O	1.0	1.3	1.2		1.0	0.8	1.3	1.3	1.3	1.0	1.2	1.5	1.2	1.4	1.2	1.3	1.2	1.3	1.5	1.4
P_2O_5	0.1	0.3	0.2		0.1	0.2	0.4	0.4	0.2	0.2	0.4	0.3	0.3	0.4	0.2	0.3	0.2	0.3	0.4	0.3
Total	99.3	98.8	101.1		99.6	101.9	100.1	100.4	98.5	100.2	99.6	101.7	100.3	99.8	100.6	98.8	99.0	100.4	99.7	99.5
F	311			314	299		425		431		431		431	446	384	454				
Cl	617			643	670		971		1076		1111		1055	1088	886	1109				
S	657			861	1337		1934		2153		1495		1865	1402	945	1991				
B		<20.5	<22.2	14.4	<16	13.4	<12.6	<15.5	<8.5		17.5	9.1	9.7	<7.8	<17.4			21.2		<16.4
Sc		15.8	8.7	18.8	36.4	37.1	7.9	11.7	12.6		13.5	22.0	9.1	13.7	6.5			13.2		6.9
V		276	218	212	293	289	259	241	218		259	235	242	228	241			250		261
Rb		24.6	27.4	22.4	19.8	16.0	17.6	17.6	17.3		18.0	21.6	17.4	20.9	16.9			21.7		21.0
Sr		447	490	446	408	364	761	755	707		746	818	754	755	744			778		857
Y		14.4	14.0	11.7	16.3	18.5	13.7	12.2	12.7		13.4	13.2	13.2	14.0	13.6			15.2		14.0
Zr		71.0	63.4	56.0	48.4	64.1	104.3	94.2	92.6		91.1	103.6	97.4	104.5	96.3			113.5		122.4
Nb		2.4	2.4	1.8	1.8	1.8	6.1	5.2	5.0		5.7	6.2	5.4	5.6	5.7			6.4		6.8
Ba		449	505	499	480	439	526	506	505		496	560	500	542	488			543		661
La		6.8	7.0	5.6	5.1	5.4	14.7	13.7	13.8		13.9	15.6	14.1	15.2	14.6			15.5		18.0
Ce		15.5	15.2	11.7	11.2	11.9	33.6	31.4	29.9		32.8	33.8	30.7	32.2	29.8			34.1		40.1
Pr		2.0	1.9	1.5	1.5	1.6	4.3	4.0	3.8		3.9	4.3	3.9	4.3	4.0			4.3		5.4
Nd		9.1	9.7	7.0	7.0	8.4	18.8	17.4	17.0		16.6	18.3	16.9	19.0	17.6			18.0		25.6
Sm		2.7	1.7	1.6	1.8	2.3	4.9	4.1	3.8		4.0	4.5	3.9	3.9	4.1			3.9		3.5
Eu		0.9	0.8	0.6	0.7	0.9	1.4	1.0	1.3		1.1	1.2	1.2	1.3	1.4			1.3		1.6
Gd		2.3	2.6	1.8	2.2	3.0	3.4	2.9	3.0		3.5	3.0	3.6	3.3	3.4			3.5		5.2
Tb		0.4	0.5	0.3	0.3	0.4	0.5	0.5	0.4		0.5		0.5	0.5	0.4			0.5		0.6
Dy		3.2	2.8	2.1	2.5	2.9	3.3	2.6	2.7		2.5	2.6	2.6	2.8	2.7			3.0		3.7
Ho		0.6	0.5	0.4	0.7	0.6	0.6	0.4	0.4		0.6		0.5	0.5	0.5			0.6		0.7
Er		1.6	1.1	1.5	1.9	1.9	1.4	1.5	1.4		1.6		1.2	1.3	1.3			1.3		2.0
Tm		0.2	0.3	0.2	0.3	0.3	0.2	0.2	0.1		0.2		0.2	0.2	0.1			0.2		0.2
Yb		1.7	1.3	1.3	2.2	2.1	1.3	1.0	1.0		1.3	1.6	1.1	1.4	1.0			1.4		1.4
Lu		0.3	0.2	0.2	0.3	0.3	0.2	0.2	0.2		0.2	0.2	0.2	0.2	0.1			0.2		0.1
Th		1.7	1.3	1.3	1.0	1.2	1.9	2.0	1.9		1.7	2.0	2.1	2.4	1.9			2.4		2.5
Pb		5.5	4.4	4.9	5.1	3.9	6.7	7.2	6.5		6.0	6.3	6.0	7.4	5.1			7.3		7.8
U		1.1	0.7	0.6	0.5	0.4	0.7	0.6	0.7		0.6	0.7	0.7	0.8	0.7			0.9		0.7
Hf		2.1	1.8	1.5	1.8	1.7	2.8	2.8	2.3		2.3	2.4	2.5	2.8	2.5			3.0		3.0
Ta		0.3	<0.16	0.1	0.1	0.2	0.2	0.3	0.2		0.2	0.3	0.2	0.3	0.2			0.3		0.3
Fo	84.6	85.5	84	82	82	85.4	85.2	83.6	84.3	84.3	86.3	85.1	85.1	84.9	84.7	84.8	84.7	84.7	85.6	85.6

Table 3 continued

	RIO10B			***Sangay*** *SAN21B*															
	5B	5C	6B	1A_b	1A_s	1B	1C	2A	2B	2C	3B	3C	4A	4B	5A	5B_m	5B_t	6A	6B	7B
SiO_2	50.4		52.3	47.9	47.0	49.2	48.9	46.5	49.7	48.5	48.6	49.3	48.0	49.3	49.8	48.1	51.3	48.5	49.9	
TiO_2	1.3		1.1	1.4	1.5	1.1	1.3	1.2	1.2	1.3	1.2	1.4	1.3	1.1	1.2	1.3	1.0	1.1	1.0	
Al_2O_3	19.3		19.2	18.3	19.2	19.5	16.9	18.5	18.3	19.3	18.9	19.2	19.1	19.2	19.8	19.6	18.6	17.7	18.9	
FeOt	6.8		7.5	8.0	7.5	6.5	6.6	7.9	6.5	6.9	7.2	6.5	6.8	6.5	6.1	7.3	6.1	8.0	6.3	
MnO	0.1		0.1	0.1	0.1	0.1	0.1	0.1	0.1	0.1	0.1	0.1	0.1	0.1	0.1	0.1	0.1	0.1	0.1	
MgO	7.0		5.5	8.5	8.6	8.0	8.6	9.4	7.7	7.7	8.9	6.9	8.2	7.6	7.1	7.8	7.4	9.6	8.0	
CaO	9.3		8.3	10.3	10.5	8.4	12.7	12.0	11.0	10.6	9.4	10.4	10.9	9.7	9.0	10.6	9.1	9.3	7.9	
Na_2O	4.0		4.4	4.1	4.2	4.6	3.6	2.6	3.9	4.0	3.9	4.3	4.0	4.5	4.7	3.8	4.4	4.0	4.4	
K_2O	1.2		1.3	1.0	1.0	2.0	1.1	1.4	1.2	1.2	1.4	1.3	1.1	1.6	1.9	1.1	1.6	1.4	2.8	
P_2O_5	0.5		0.2	0.4	0.4	0.5	0.3	0.3	0.4	0.4	0.4	0.6	0.4	0.4	0.3	0.3	0.3	0.3	0.8	
Total	100.6		100.2	101.1	99.9	99.8	100.3	98.1	100.3	100.6	100.6	100.3	99.3	100.2	99.3	99.3	100.3	99.8	100.2	
F	452	491		407			381		428	424	408	432	386	435	466		409	405	487	321
Cl	1115	1244		801			672		833	809	777	837	695	844	1127		923	784	1991	503
S	1311	2581		1147			825		966	734	985	979	846	802	768		562	1057	728	706
B		<15.4	<20.3	5.8		10.7		<8.7		12.5		<15.6	9.8	9.7	<7.1			11.9	10.5	
Sc		5.8	13.9	24.3		12.9		25.5		18.0		19.0	20.3	17.9	16.6			20.8	14.3	
V		300	239	283		207		275		261		255	273	228	203			221	247	
Rb		19.9	22.5	17.2		25.1		25.5		19.9		24.4	15.8	27.8	34.1			22.3	11.5	
Sr		891	685	865		1441		937		846		919	788	907	1096			842	841	
Y		14.9	14.2	17.9		13.0		18.4		15.3		15.6	15.2	14.7	14.4			14.5	14.0	
Zr		109.4	109.0	98.3		87.7		100.1		83.1		87.2	85.5	91.9	103.5			86.7	85.8	
Nb		6.4	6.1	6.2		6.7		8.3		5.5		5.9	5.1	6.2	7.8			5.5	5.3	
Ba		578	499	558		1006		566		557		599	485	673	835			586	463	
La		16.6	14.0	14.8		27.2		19.4		14.6		15.7	13.0	16.4	23.7			15.2	14.7	
Ce		36.1	30.9	34.3		55.0		42.4		32.8		33.5	28.9	35.2	48.4			32.7	33.2	
Pr		4.3	3.8	4.5		6.7		5.7		4.2		4.6	4.0	4.6	6.1			4.3	4.5	
Nd		21.1	17.0	20.6		27.2		24.9		19.8		19.3	19.0	19.7	26.3			19.5	21.4	
Sm		4.5	4.0	5.2		5.1		5.7		4.0		4.2	3.9	4.1	5.6			4.3	4.6	
Eu		1.5	1.3	1.5		1.4		1.8		1.3		1.3	1.4	1.2	1.4			1.3	1.4	
Gd		3.6	3.4	4.4		3.2		4.2		3.4		4.1	3.7	3.7	4.0			3.7	3.9	
Tb		0.5	0.4	0.6		0.4		0.5		0.5		0.6	0.5	0.5	0.5			0.5	0.5	
Dy		2.9	2.9	3.7		2.5		3.8		3.2		3.1	3.1	3.2	3.0			2.8	2.9	
Ho		0.5	0.6	0.6		0.4		0.7		0.6		0.7	0.6	0.5	0.5			0.5	0.6	
Er		1.3	1.5	1.6		1.2		1.9		1.6		2.0	1.7	1.6	1.6			1.6	1.5	
Tm		0.1	0.2	0.2		0.2		0.3		0.2		0.1	0.2	0.2	0.2			0.2	0.2	
Yb		1.2	1.1	1.7		1.3		1.7		1.4		1.5	1.3	1.4	1.4			1.3	1.2	
Lu		0.2	0.2	0.2		0.2		0.3		0.2		0.2	0.2	0.2	0.2			0.2	0.2	
Th		2.1	2.2	2.7		4.3		3.6		2.2		2.5	1.9	2.8	4.8			2.8	1.9	
Pb		7.3	21.9	6.1		5.8		<0.11		3.9		4.0	3.8	5.3	6.5			6.1	2.0	
U		0.8	0.8	0.8		1.1		1.1		0.7		0.8	0.5	1.0	1.5			0.8	0.6	
Hf		3.0	2.9	2.6		2.3		2.6		2.3		2.7	2.3	2.8	3.0			2.3	2.4	
Ta		0.3	0.3	0.3		0.3		0.4		0.3		0.5	0.2	0.3	0.4			0.3	0.3	
Fo	85.4	85.2	84.1	82.9	83.4	83.2	83.4	83.7	82.6	81.9	81.2	83	83.6	81.3	82.3	82.2	82.2	81.4	82.6	

Table 4 Some major, volatile and incompatible trace element ratio values for Ecuadorian olivine-hosted MI.

	Hosting olivine				Melt inclusions by groups						
Volcano	**Sample**	**Forsterite content**	**Fo>80**	**Fo>85**	**K_2O/Na_2O**	**F/Cl**	**B/Nb**	**Pb/Ce**	**Ba/La**	**Ba/Th**	**Reference**
Cotacachi	17EQ91 MM1B COTA02	84.3-87.9	15	12	0.24 (0.04) **0.24**	0.36 (0.03) **0.36**	10.4 (4.4) **9.3**	0.22 (0.06) **0.22**	79.6 (16.1) **76.7**	640 (212) **628**	*this work*
Cubilche	17EQ81 17EQ95	80.4-88.3	17	10	0.27 (0.03) **0.27**	0.45 (0.05) **0.42**	9.1 (4.9) **9.8**	0.3 (0.1) 0.28	76.5 (12.7) **75.6**	399 (103) **402**	*this work*
Conos de Licto	RIO10B	83.6-86.3	18	9	0.3 (0.02) **0.3**	0.41 (0.02) **0.4**	2.4 (0.7) **2.3**	0.24 (0.14) **0.19**	35.8 (1.0) **35.9**	256 (20) **266**	*this work*
Sangay	SAN21B	81.2-83.7	17	0	0.35 (0.1)	0.5 (0.09)	1.7 (0.6)	0.12 (0.05)	36.3 (3.6)	222 (34)	*this work*
	SAN20B	86.8-89.0	8	8	0.29 (0.01) **0.29**	0.42 (0.05) **0.42**	1.1 (0.5) **1.1**	0.15 (0.01) **0.15**	29.3 (1.6) **29.3**	261 (17) **261**	Narváez et al. (2018)
Rucu Pichincha		86.2-89.1	38	38	0.25 (0.01) **0.25**	0.42 (0.06) **0.42**	7.9 (2.5) **7.9**		66.9 (17.1) **66.9**		Le Voyer et al. (2008)
Cono de la virgen	CAY45A CAY45B CAY45C	86.3-89.9	18	18	1.94 (0.8) **1.94**	5.22 (1.72) **5.22**	1.5 (0.9) **1.5**	0.07 (0.02) **0.07**	19.6 (5.8) **19.6**	98 (32) **98**	*this work*
Puñalica		82.4-85.8	42	5	0.41 (0.04) **0.41**	0.19 (0.08) **0.14**	2.0 (0.7) **0.73**	0.13 (0.05) **0.15**	23.6 (20.8) **22.5**	108 (102) **104**	Narváez et al. (2018)
PDA		78-88.2	17	7	0.4 (0.03) **0.39**	0.72 (0.24) **0.83**	0.4 (0.1)		26.1 (2.3)		Le Voyer et al. (2008)

Note. Forsterite content is calculated as 100*molar (MgO/(MgO+FeOT)). The Fo>80 and Fo>85 columns represent the number of MI hosted in olivines with a forsterite content greater than 80 and 85, respectively. Values in parentheses are 1σ (standard deviation) of mean values. Bold type values are mean values calculated for MI hosted in Fo>85 olivines. Nb/Nb* is Nb content of MI normalized to NMORB (Sun & McDonough, 1989) divided by Nb* where log(Nb*) = ((log(U)+log(K))/2).

Table 4 continued

	Melt inclusions by groups								
Volcano	**Sample**	**$(La/Yb)_N$**	**Th/Nb**	**Th/La**	**La/Nb**	**Nb/Nb***	**Hf/Nb**	**Zr/Nb**	**Reference**
Cotacachi	17EQ91 MM1B COTA02	1.7 (0.6) **1.7**	0.35 (0.1) **0.33**	0.13 (0.02) **0.13**	2.7 (0.3) **2.6**	0.08 (0.01) **0.08**	1.0 (0.2) **0.97**	35 (7.7) **33.2**	*this work*
Cubilche	17EQ81 17EQ95	2.8 (1.3) **2.6**	0.57 (0.1) **0.56**	0.2 (0.03) **0.19**	2.9 (0.2) **2.9**	0.06 (0.01) **0.08**	0.89 (0.14) **0.91**	31.9 (5.4) **33.7**	*this work*
Conos de Licto	RIO10B	8.4 (1.0) **8.4**	0.36 (0.03) **0.36**	0.14 (0.01) **0.14**	2.6 (0.1) **2.6**	0.14 (0.01) **0.15**	0.46 (0.04) **0.44**	17.5 (0.7) **17.2**	*this work*
Sangay	SAN21B	8.6 (2.5)	0.46 (0.1)	0.17 (0.02)	2.8 (0.5)	0.12 (0.02)	0.41 (0.05)	14.8 (1.5)	*this work*
	SAN20B*	10.7 (2.6) **10.7**	0.19 (0.01) **0.19**	0.11 (0.00) **0.11**	1.7 (0.1) **1.7**	0.35 (0.14) **0.35**	0.2 (0.02) **0.2**	7.2 (0.8) **7.2**	Narváez et al. (2018)
Rucu Pichincha		2.7 (0.7) **2.7**			3.3 (1.6) **3.3**			47.7 (21.2) **47.7**	Le Voyer et al. (2008)
Cono de la virgen	CAY45A CAY45B CAY45C	75.8 (24.1) **75.8**	2.7 (0.5) **2.7**	0.2 (0.03) **0.2**	13.4 (2.2) **13.4**	0.04 (0.01) **0.04**	0.96 (0.12) **0.96**	37.7 (4.1) **37.7**	*this work*
Puñalica		19.3 (9.2) **13.3**	2.1 (0.7) **1.56**	0.22 (0.02) **0.22**	9.7 (1.6) **7.3**	0.04 (0.01) **0.05**	0.63 (0.1) **0.58**	24.5 (2.7) **22.8**	Narváez et al. (2018)
PDA		13.1 (2.6)			2.2 (0.6)			7 (2.5)	Le Voyer et al. (2008)

Table 5 Geochemical model parameters used to reproduce Cotacachi, Sangay, Cubilche, and CLV MI compositions.

Volcano/sample	Aqueous fluid (A)-Siliceous melt (M)	Slab addition (mass %)	Degree of mantle melting (%)	Garnet (vol. %)	P (GPa) mantle melting	Slab fluid/melt fraction			% melting	
						Fliq (SED)	Fliq (AOC)	Fliq (DMM)	SED	AOC
Cotacachi/ MM1B_1B	A	1	5	0.6	2	0	1	0		
Sangay/ SAN21B_4B, Licto/ RIO10B_2A	A	2.5	5	4.1	2.5	0.3	0.7	0		
Cubilche/ 17EQ81_3C_b	A	1	5	1.4	2.2	0.1	0.9	0		
CLV/ CAY45C_5A	M	15	5	2.7	1.8	0.25	0.75	0	15	10
CLV/ CAY45C_5A	M and phlogopite (7%)	15	5	6.1	2.2	0.16	0.64	0.2	15	10
Puñalica	M	5	5	2.4	2.2	0.25	0.75	0	15	10

Note. The model parameters for Licto are similar to those shown for Sangay. MI from CLV and Puñalica are modelled with a hydrous siliceous melt, unlike all the other MI that are modelled with an aqueous fluid-like component. The parameter for CLV MI using phlogopite in the residue is also shown. The slab liquid fraction refers to either aqueous fluid or siliceous melt coming from sediments (SED), altered oceanic crust (AOC), or depleted mantle (DMM) making up the subducted slab.